Anti-localisation suppresses nonradiative recombination in GaInN/GaN quantum wells

Andreas Hangleiter, Carsten Netzel, Daniel Fuhrmann, Frank Ferdinand Hitzel, Lars Hoffmann, Heiko Bremers, Uwe Rossow, George Ade, Peter Hinze

Anti-localisation suppresses nonradiative recombination in GaInN/GaN quantum wells

Journal:	*Philosophical Magazine & Philosophical Magazine Letters*
Manuscript ID:	TPHM-06-Jul-0273.R2
Journal Selection:	Philosophical Magazine
Date Submitted by the Author:	14-Dec-2006
Complete List of Authors:	Hangleiter, Andreas; Technical University of Braunschweig, Institute of Applied Physics Netzel, Carsten; Technical University of Braunschweig, Institute of Applied Physics Fuhrmann, Daniel; Technical University of Braunschweig, Institute of Applied Physics Hitzel, Frank; Technical University of Braunschweig, Institute of Applied Physics Hoffmann, Lars; Technical University of Braunschweig, Institute of Applied Physics Bremers, Heiko; Technical University of Braunschweig, Institute of Applied Physics Rossow, Uwe; Technical University of Braunschweig, Institute of Applied Physics Ade, George; Physikalisch Technische Bundesanstalt Hinze, Peter; Physikalisch Technische Bundesanstalt; Physikalisch Technische Bundesanstalt
Keywords:	GaN, low-dimensional structures, luminescence, microstructure, quantum wells, scanning probe microscopy, semiconductors, TEM
Keywords (user supplied):	luminescence efficiency, InGaN
Note: The following files were submitted by the author for peer review, but cannot be converted to PDF. You must view these files (e.g. movies) online.	

Hangleiter_PhilMag_rev2col.tex
Hangleiter_PhilMag_rev2col.bbl

Philosophical Magazine,
Vol. 00, No. 00, DD Month 200x, 1–19

Anti-localisation suppresses nonradiative recombination in GaInN/GaN quantum wells

A. Hangleiter, C. Netzel, D. Fuhrmann, F. Hitzel, L. Hoffmann, H. Bremers, and U. Rossow

Institute of Applied Physics, Technical University of Braunschweig
Mendelssohnstrasse 2, D-38106 Braunschweig, Germany

G. Ade and P. Hinze

Physikalisch-Technische Bundesanstalt
Bundesallee 100, D-38116 Braunschweig, Germany

(21 July 2006)

The light emission efficiency of (AlGaIn)N heterostructures and light emitting diodes is exceptionally high, despite the high density of threading dislocations generally found in such structures. It has become common to attribute the high efficiency to compositional fluctuations or even phase separation in the active GaInN quantum well region. The resulting localisation of charge carriers is thought to keep them from recombining nonradiatively at the defects. Here, we show that carriers are mobile at room temperature rather than localised and that under suitable growth conditions hexagonal V-shaped pits decorating the defects exhibit narrow sidewall quantum wells with an effective bandgap significantly larger than that of the regular c-plane quantum wells. Thereby nature provides a unique, hitherto unrecognised mechanism generating a potential landscape which effectively screens the defects themselves by providing an energy barrier around every defect. Thus even for mobile charge carriers nonradiative recombination is effectively suppressed leading to the unexpectedly high emission efficiency.

1 Introduction

Quantum wells based on (AlGaIn)N heterostructures are now being widely applied for todays high-brightness violet, blue, and green light emitting diodes [1]. Presently, the emission wavelength of such quantum wells and LED's is being pushed forward towards much shorter wavelength. For In-containing structures emitting in the visible and near UV range, a high emission efficiency is achieved despite of the large defect density of the material associated with the heteroepitaxial growth of nitrides on foreign substrates [2]. On the other hand, In-free structures for UV emission so far suffer from insufficient light output levels.

Light emission from semiconductors and semiconductor heterostructures is subject to competition between radiative and nonradiative recombination of electron-hole pairs. Only for highly perfect crystalline material with a low number of "deep" defect states, the nonradiative recombination probability is low enough to allow for a significant fraction of the electron-hole pairs to recombine radiatively.

In fact, conventional semiconductor wisdom "knows" that significant numbers of structural imperfections and defects either prohibit light emission at all or make the structures degrade quickly. For instance, in AlGaInP-based red LED's a dislocation density of more than $10^3\mathrm{cm}^{-2}$ reduces the radiative efficiency by more than an order of magnitude.

This was the background when in 1994 Nakamura *et al.* [3] reported their first blue LED exceeding one candela in brightness. The device was made from a GaInN/GaN heterostructure epitaxially grown on a highly dissimilar substrate, namely sapphire. Due to the 30 % difference in lattice constant, a large number (up to $10^{10}\mathrm{cm}^{-2}$) of "threading dislocations" running along the (0001) growth direction plagues the material and intersects the active light emitting layers [2]. As for a "normal" semiconductor one would not expect any light emission at all at such high defect density, the high brightness even of these early devices was highly surprising. Later on, even higher efficiency was obtained using quantum well active regions [1, 4].

Philosophical Magazine
ISSN 1478-6435 print/ISSN 1478-6443 online © 200x Taylor & Francis
http://www.tandf.co.uk/journals
DOI: 10.1080/1478643YYxxxxxxxx

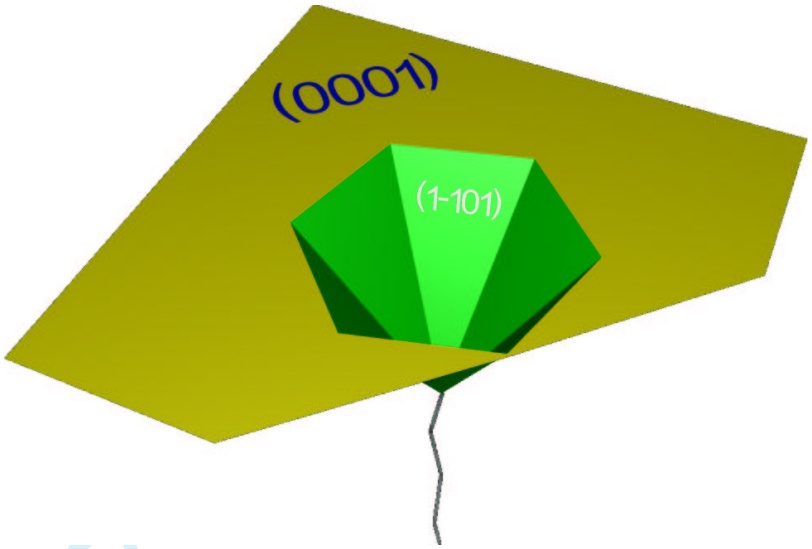

Figure 1. Schematic view of a hexagonal V-shaped pit emerging at the apex of a threading dislocation in a GaInN-based heterostructure.

As the active GaInN layers exhibited optical properties highly unusual for III-V semiconductors [5, 6], it was suggested that excitons localised at compositional fluctuations or even quantum dots play a dominant role [7, 8]. This kind of random localisation of excitons was proposed to prohibit nonradiative recombination of the excitons at threading dislocations [7]. It appeared to be supported by transmission electron microscope (TEM) images showing small dot-like structures [9]. On the other hand, recent detailed TEM studies indicate that such dot-like structures may be artifacts due to radiation damage during TEM observation [10].

As far as the optical properties were concerned, however, it was soon recognised that due to the lattice mismatch between GaInN and GaN (or between GaN and AlGaN) and the resulting pseudomorphic strain field the highly polar lattice leads to a strong piezoelectric polarisation [11] inside the quantum wells. The huge internal field (of the order MV/cm [12]) in turn gives rise to a strong "quantum confined Stark effect" (QCSE) first observed in GaAs-based quantum wells [13]. In addition to a strong red-shift of the emission [14], a dramatic reduction of the oscillator strength may thus result from these fields [15, 16]. In fact, most of the unusual optical properties of nitride quantum wells may be well understood on the basis of the polarisation fields [17]. However, the internal fields alone provide no explanation of the unusually large emission efficiency of such structures, even though they may enhance the effect of fluctuations [18]. On the contrary, one might expect an even smaller efficiency due to the reduced oscillator strength.

Epitaxial growth of group-III nitrides by means of metal-organic vapour phase epitaxy (MOVPE) typically requires growth temperature in excess of 1000^oC [19], due to the large binding energies of the species involved. At lower temperature and at low V-III ratio, the epitaxial layers tend to grow in a faceted manner. In other words, in order to achieve smooth planar surfaces, high temperature and large V-III ratio is required.

However, if In is to be incorporated into the layers, the low binding energy of InN and the large vapour pressure of N forces the use of much lower temperatures, typically around 800^oC. At such low temperatures, even small perturbations of the surface tend to grow into (inclined) facets with the lowest growth rate, i.e. $(1\bar{1}01)$ facets. This is particularly true at the apex of threading dislocations, where V-shaped hexagonal pits with $(1\bar{1}01)$ sidewalls appear [20–22] (c.f. Fig. 1). Using atomic force microscopy (AFM), one realizes that under suitable conditions virtually every threading dislocation is decorated with such a pit.

If thick layers of GaInN are grown, the pits become very large and finally cover the whole surface. In incorporation in the faceted area increases and a strongly inhomogeneous composition results [23]. In case of thin GaInN quantum wells with thicknesses of 5 nm and less, growth remains regular and well defined pits evolve for multiple quantum well structures [21, 22].

In this paper, we discuss systematic studies of the correlation of luminescence efficiency and microstructure of GaInN/GaN quantum wells. Using quantitative measurements of internal efficiency combined with

highly resolved near-field microscopy and transmission electron microscopy we demonstrate that even in the highest efficiency samples, excitons are mobile at room temperature but are prohibited from recombining nonradiatively at threading dislocations by potential barriers around every dislocation thanks to narrow quantum wells formed on the facets of V-shaped pits decorating the dislocations.

2 Experimental

Our quantum well samples were grown by low pressure metalorganic vapour phase epitaxy (MOVPE) in a horizontal reactor (Aixtron 200 RF). GaInN/GaN single and double QW's with various well widths were grown on c-plane sapphire substrates after growing a 1.7 μm thick nominally undoped GaN buffer layer on the nucleation layer. A cap GaN layer of 100 nm thickness was deposited on an AlGaN electron blocking layer on top of the GaInN/GaN QW's. For all samples buffer, electron blocking, and capping layers were virtually the same. These layers were grown using Trimethylgallium (TMGa), Trimethylaluminum (TMAl) and ammonia (NH3) as precursors and H_2 as carrier gas at 100mbar. The growth temperature was 1180 ^{o}C and 1100 ^{o}C (uncorrected thermocouple reading) for GaN buffer and capping layer/electron blocking layer, respectively. After some initial experiments with TMGa and Trimethylindium (TMIn), the GaInN QWs were grown with Triethylgallium (TEGa) and Trimethylindium (TMIn) as precursors, N_2 as carrier gas and a total pressure of 200 mbar, in order to ensure slow, high quality growth of the QW's. The growth temperature was varied between 740 ^{o}C and 850 ^{o}C in order to adjust the desired In composition. The V/III-ratio was about 1350 for the buffer and cap layers and about 3750 for the quantum wells. The growth rates were 1.7 μm/h for the buffer and 110 nm/h for the QW region. Further details on growth optimisation and its impact on the device efficiency can be found elsewhere [24].

The In content of the GaInN QW layers (10 - 20 %) and the QW and barrier width were determined by high-resolution X-ray diffraction (HXRD) on multiple quantum well (MQW) samples. The QW width was varied on the range 1 - 5 nm and the undoped GaN barrier was kept constant at a width of 7 nm. Cross-sectional transmission electron microscopy (TEM) was carried out in a Philips CM 200 FEG or in a Zeiss Leo 922 microscope both operated at 200 kV.

The samples were mounted in a Helium cryostat for variable-temperature photoluminescence (PL) measurements. The PL was measured by using an Ar-Ion laser (380 nm) as a resonant excitation source with various excitation power levels. The internal quantum efficiency at room temperature was determined from the temperature and power dependence of the integrated quantum well PL intensity, normalised to the excitation power. The largest value in this two-dimensional data set is then normalised to unity. This procedure is based on the assumption that nonradiative recombination is negligible at low temperatures. If saturation of the efficiency both at low temperature and at high excitation power occurs, such a procedure may be assumed to be justified. In fact, comparison with external efficiencies under electrical injection using model calculations for the extraction efficiency also verifies these assumptions [24].

Spatially resolved luminescence measurements were performed using a low-temperature scanning near-field optical microscope (SNOM) attached to a spectrometer equipped with a liquid-nitrogen cooled charge-coupled-device (CCD) detector, running in illumination-collection mode. The SNOM can be operated both at low temperature (20 K) or at room temperature. Fiber probes were home-made using a tube-etching process and metal-coated with aluminium. Optical excitation during SNOM measurements was performed using the 335 nm line of an Ar-ion laser. Typical SNOM measurements consist of scanning 128x128 points on a 5x5 μm area, collecting a complete emission spectrum at each point. The spatial resolution obtained with our instrument was better than $\lambda/10$ under optimum conditions, the spectral resolution was set to about 1.5 nm.

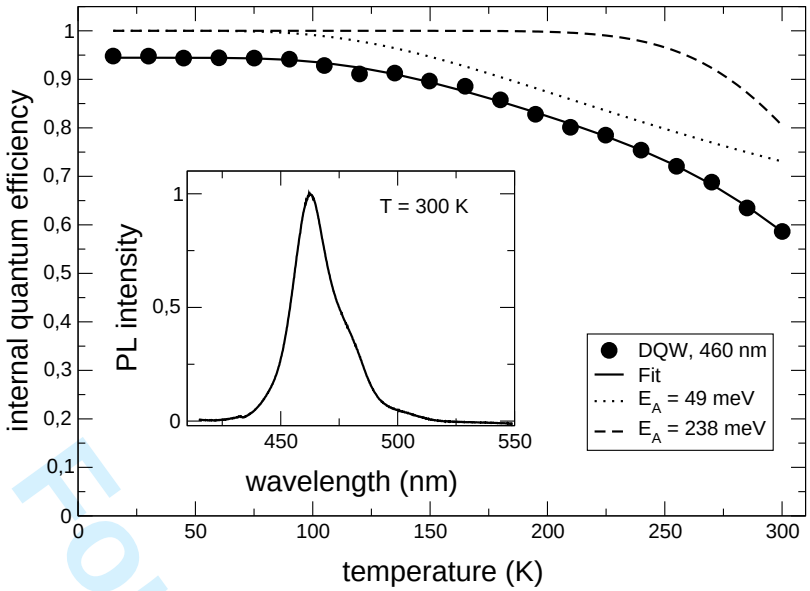

Figure 2. Dependence of the internal quantum efficiency of a 2 nm GaInN/GaN DQW sample ($\lambda_{em} \approx 460$ nm) on temperature, measured at an absorbed power density of about 20 W/cm^2. The full line represents a fit with the phenomenological model described in the text, the broken lines show the two components of the fit. The inset depicts the PL spectrum at room temperature, which represents a fairly narrow linewidth, as evident from the phonon replicas. (Note: The power dependence of the efficiency for this sample is shown in Fig. 7.)

3 Efficiency analysis

The internal quantum efficiency is defined as

$$\eta_{\rm int} = \frac{R_{\rm rad}}{R_{\rm rad} + R_{\rm loss}} = \frac{R_{\rm rad}}{R_{\rm tot}}, \tag{1}$$

i.e. as the ratio of the radiative recombination rate and the total recombination rate.

A typical case for the temperature dependence of the internal efficiency of a highly efficient sample is shown in Fig. 2. Clearly, the efficiency is constant and close to unity below about 100 K, justifying the quantitative interpretation as the internal quantum efficiency. At higher temperatures, the efficiency decreases and reaches about 60 % at room temperature.

In order to assess the temperature dependence on a phenomenological basis, we assume that the losses are due to recombination via excited states, as these losses occur at higher temperature only. This assumption even accounts for classical nonradiative processes involving an activation barrier [25]. For the present purpose, we use three excited states with occupation numbers n_2, n_3, and n_4, and corresponding lifetimes τ_2, τ_4, τ_4. The ground state occupation number and lifetime are denoted by n_1 and τ_1.

$$\eta_{\rm int} = \frac{n_1/\tau_1}{n_1/\tau_1 + n_2/\tau_2 + n_3/\tau_3 + n_4/\tau_4} \tag{2}$$

$$= \frac{1}{1 + \frac{n_1}{n_2}\frac{\tau_2}{\tau_1} + \frac{n_1}{n_3}\frac{\tau_3}{\tau_1} + \frac{n_1}{n_4}\frac{\tau_4}{\tau_1}} \tag{3}$$

While the lifetime ratios $\frac{\tau_1}{\tau_i}$ may be taken as constants for the time being, the occupation ratios are given by

$$\frac{n_1}{n_i} = \frac{g_1}{g_i} e^{-\frac{E_i - E_1}{kT}}, \tag{4}$$

where g_i are the degeneracies, which may itself depend on temperature in case of extended (band) states. In particular, $g_i \propto T^{3/2}$ for bulk-like states, and $g_i \propto T$ for two-dimensional states.

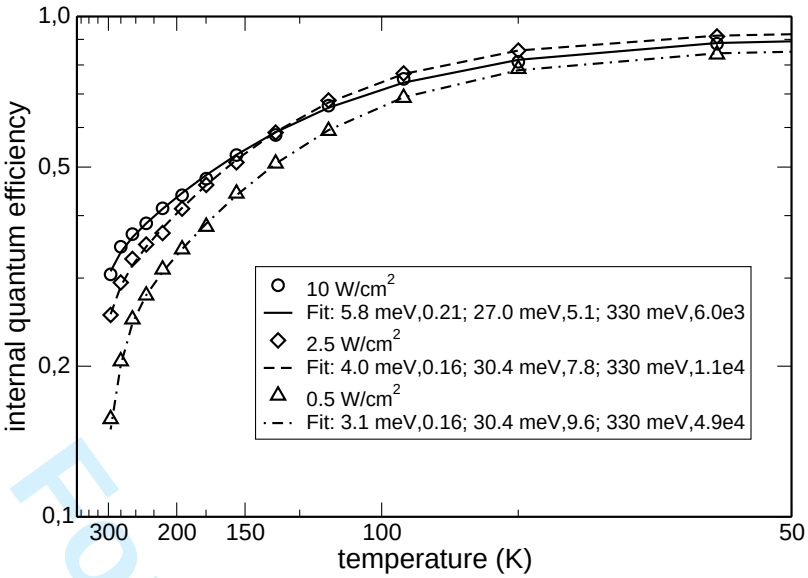

Figure 3. Detailed analysis of the temperature dependent efficiency of a 3 nm GaInN/GaN DQW sample, emitting at 440 nm. This particular sample has only 30 % room temperature efficiency, but is used to illustrate the interplay of activation energies. Three activation energies were used in the fit, the energies and weights are given in the figure.

The temperature dependence can now be described by a thermal activation law like

$$\eta_{int}(T) = \frac{\eta_0}{1 + c_1 e^{-\frac{E_1}{kT}} + c_2 e^{-\frac{E_2}{kT}} + c_3\sqrt{T} e^{-\frac{E_3}{kT}}}. \quad (5)$$

In this particular case (Fig. 2) we use only two activation energies yielding values of 49 and 238 meV . The prefactors of the exponentials reflect the density of states ratio, e.g. thermal emission from a 2D state to a 3D state has a prefactor of $T^{1/2}$.

The thermally activated behaviour can be generally attributed either to thermally activated nonradiative processes or to excitation to higher levels such as thermal emission out of the QW.

3.1 *Analysis of temperature dependence*

The procedure outline above has been applied to large set of samples, whose temperature dependent efficiency was measured for various excitation powers. Generally, we find that within reasonable limits, the activation energies are independent of excitation power density. Only the prefactors change significantly with power. This is illustrated in Fig. 3 for a 3 nm GaInN/GaN double quantum well using three activation energies. One can clearly see that the activation energies are constant (except possibly for the smallest one), while the weights of the activation terms change with excitation power density.

Looking at samples with various well widths, well compositions, and emission wavelengths we actually find two or three significant activation energies. All of these fall into three groups of activation energies: i) a large activation energy in the range 100 - 350 meV, ii) a second group comprising values between 25 and 60 meV, and iii) a small activation energy of 1 - 15 meV.

The largest of the set of activation energies exhibits a characteristic dependence on emission wavelength as shown in Fig. 4. Within the error limit, the activation energy is equal to half the total confinement energy, i.e. one half of the difference in bandgap between the QW and the surrounding GaN barrier. It can thus be identified with thermal emission of carriers out of the QW. Such behaviour has previously been observed in other materials [26] and relates to the fact that for charge neutrality reasons, electrons and holes are emitted from the quantum well in pairs.

The second activation energy exhibits a characteristic dependence on the width of the QW's. As shown in Fig. 5, this activation energy is large for small well thickness and tends to decrease towards larger well width. As the absolute value is in the range expected for the free exciton binding energy, we have calculated

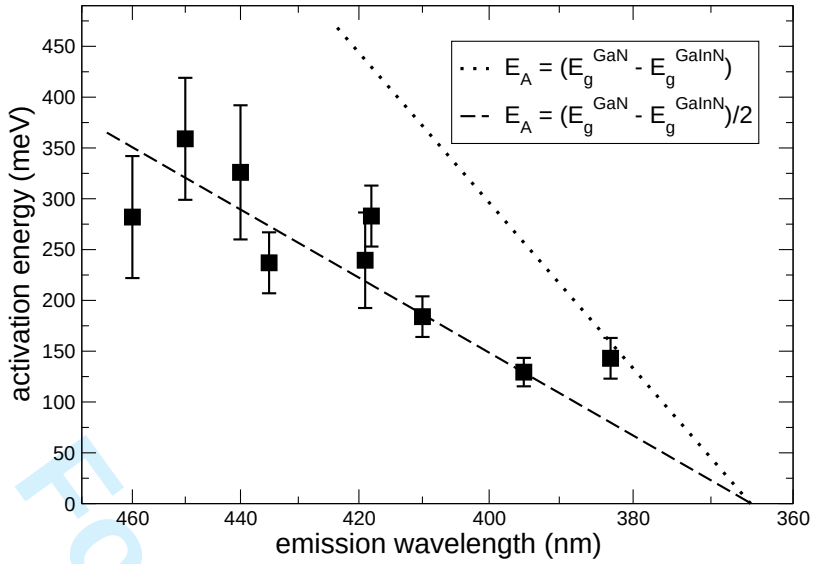

Figure 4. Largest thermal activation energy observed in the temperature dependent internal efficiency data for samples with various different room temperature emission wavelengths. The experimental data are compared with lines corresponding to the total confinement energy and to one half of the total confinement energy, respectively. A good correlation with one half of the total confinement energy is observed.

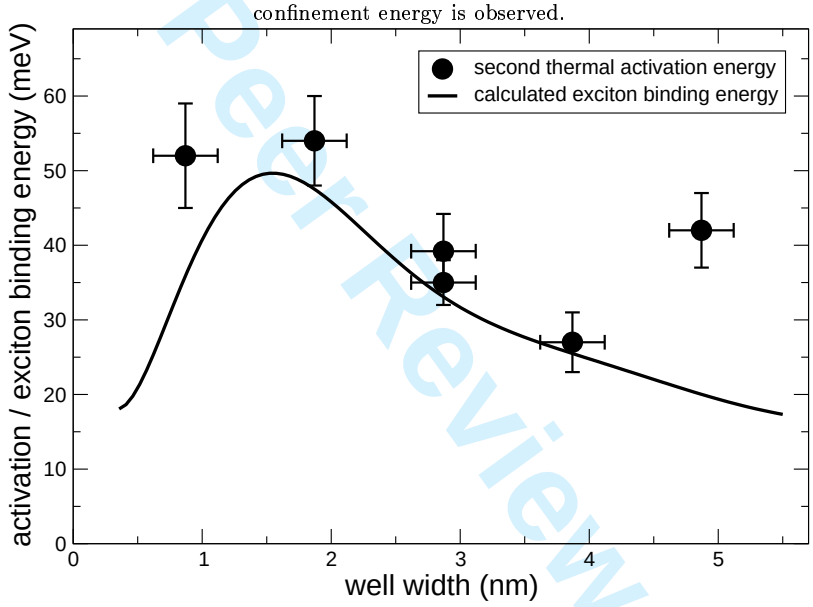

Figure 5. Second thermal activation energy of the internal efficiency vs. well width for a series of samples with varying well width. An interesting correlation to the calculated free exciton binding energy may be noticed.

the exciton binding energy as a function of well width, taking into account polarisation fields as well as the actual sample structure. Fig. 5 reveals that both the absolute value as well as the dependence on well width comes close to the observed activation energies.

The third activation energy is in the range 0 - 10 meV and scales linearly with the quantum well width [27]. The values coincide with localisation energies determined from the luminescence peak shift with temperature. Therefore we associate the smallest and least important activation energy with exciton localisation.

3.2 *Results and model for the excitation dependence*

Besides the temperature dependence, the dependence of the internal efficiency on excitation power density provides even more insight. A typical case is shown in Fig. 6, where the efficiency for several temperatures is plotted as a function of excitation power. For all temperatures, we observe a monotonous increase of

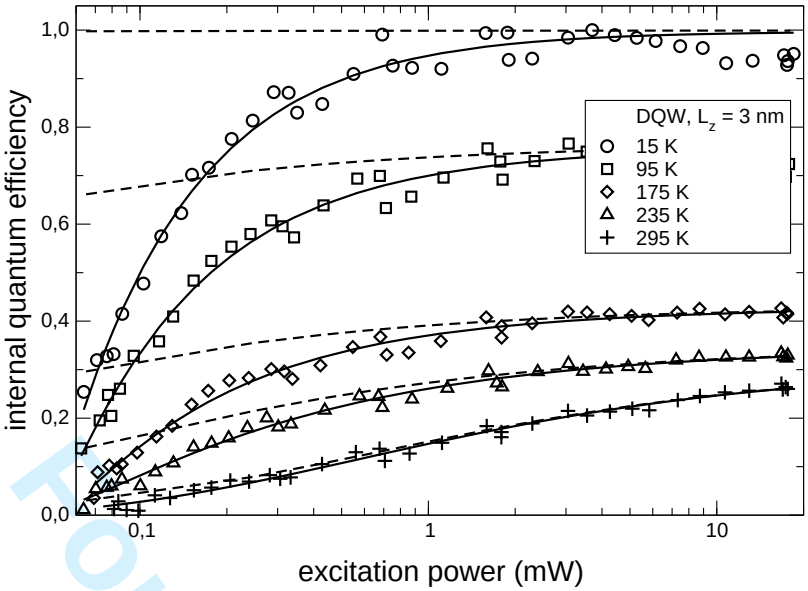

Figure 6. Dependence of the internal quantum efficiency of a 3 nm GaInN/GaN DQW sample ($\lambda_{em} \approx 440$ nm) on excitation power, measured for several temperatures (10 mW correspond to 5 W/cm^2). The full lines represent a fit with the model described in the text. The dashed lines are based on the same model, but without separate localisation of electrons and holes.

efficiency (except for the highest powers at low temperature) with increasing power level. As already seen from the temperature dependence, the maximum efficiency becomes lower at higher temperature. It is important to note, however, that even for the lowest temperature, the efficiency decreases towards low excitation power densities.

It is interesting to start the discussion by considering the case of recombination of localised excitons [5]. If the observed emission were dominated by such localised excitons, one would expect that localisation would be most effective at low carrier density, i.e. low excitation power, where essentially no filling of potential minima takes place [28]. As it is generally assumed that nonradiative recombination is ineffective only for localised carriers, the efficiency should be highest at the lowest excitation level. Obviously, our experimental observations are not consistent with this scenario. This indicates that exciton localisation is not the prevailing mechanism.

Let us now discuss an alternative model to explain the observations, based essentially on free excitons. As we are working under steady state conditions, the generation rate equals the recombination rate

$$G = R_{rad} + R_{nonrad} = \frac{x}{\tau_r} + \frac{N}{\tau_{nr}}, \quad (6)$$

where $R_{rad} = x/\tau_r$ is the radiative rate given by the free exciton density x and the exciton radiative lifetime τ_r, and $R_{nonrad} = N/\tau_{nr}$ is the nonradiative rate given by the total carrier density N and the nonradiative lifetime τ_{nr}.

In fact, we assume here that radiative recombination of free electrons and holes is negligible compared to that of excitons, which is reasonable as long as the two-dimensional carrier density is small compared to the inverse square of the exciton Bohr radius. For an exciton Bohr radius of 3 nm (bulk value [29]) the reference density would be 3.5×10^{12}cm^{-2} compared to typical carrier densities of less than 1×10^{11}cm^{-2} in our experiments.

The nonradiative rate scales linearly with the carrier density N and the defect density N_t

$$R_{nr} = c \cdot N \cdot N_t = \frac{N}{\tau_{nr}} \quad (7)$$

where c is an effective capture coefficient and N is the total carrier density given by

$$N = x + n + n_t, \tag{8}$$

where n (p) is the free electron (hole) density and n_t is a trapped electron density to be discussed below. Here, we assume that both free carriers and excitons interact with nonradiative centres. Both the radiative lifetime (of excitons) and the nonradiative lifetime may then be assumed independent of carrier density.

One should note that in the presence of piezoelectric fields the optical transitions in the QW are subject to a strong QCSE. Therefore, the oscillator strength becomes dependent on carrier density [16], due to free-carrier screening of the polarisation field. In principle, this leads to a smaller radiative lifetime of excitons at higher carrier density. However, for the narrow quantum wells considered here (≈ 2 nm) and the relatively small carrier densities ($< 1 \times 10^{11}\mathrm{cm}^{-2}$), this effect is well below a factor of two and is neglected in the initial analysis.

Finally, the relation between exciton density and free electron density is governed by a mass-action-law (in the undoped case $n = p$)

$$\frac{n \cdot p}{x} = \frac{n^2}{x} = D_r^{\mathrm{eff}}(T) \cdot e^{-\frac{E_x}{kT}} = C(T), \tag{9}$$

where $D_r^{\mathrm{eff}}(T)$ is the reduced effective density of states and E_x is the free exciton binding energy. For the present purpose, we can treat $C(T)$ as a temperature dependent constant, which, in fact, will be used as a fitting parameter further on.

This set of three equations can be combined into a cubic equation for the exciton density x as a function of generation rate. Using the (numerical) solution, the internal quantum efficiency given by

$$\eta_{int} = \frac{R_{rad}}{R_{tot}} = \frac{x}{\tau_r G} \tag{10}$$

can be calculated.

Using eq. 10 we have curve-fitted the experimental data shown in Fig. 6 and included the fit curves as full lines in the figure. As one can see, we obtain perfect agreement between our model and the experimental points. However, without the trapping term in eq. 8 (dashed lines in Fig. 6), the result would only be valid for the highest temperature. Obviously, in order to understand the strong decrease of efficiency towards low excitation at lower temperatures one needs to include an additional mechanism to reduce the radiative rate, or, in other words, the exciton density.

If we consider, as proposed by Kalliakos *et al.* [30], that electrons and holes are being trapped separately, the free electron and hole density would be reduced, leading to a more pronounced dissociation of excitons at low temperature, where trapping comes into play. Thus, we include a trapped electron term in eq. 8, which brings the model into good agreement with experiments.

In fact, one of the fitting parameters in the model is the exciton dissociation constant $C(T)$. The results (not shown) exhibit an exponential behaviour with temperature, as expected, with an exciton binding energy of 30 ± 5 meV.

A closer look at the linear plot of the data shown in Fig. 7 shows that at low temperature there appears a drop in efficiency at larger excitation power densities. Such a drop in efficiency is also frequently observed in room-temperature efficiency curves of blue and green LED's [31]. In order to explain this behaviour in the present framework, we need to go somewhat more deeply into the reasons for the low recombination activity of defects in high-efficency GaInN/GaN quantum wells. As we have recently shown [32,33], defects in such structures are surrounded by higher-bandgap regions acting as an electronic barrier preventing nonradiative exciton recombination.

In order to incorporate this into our present model, we write the nonradiative lifetime as

$$\tau_{nr} = \tau_{nr}^0 \exp^{\frac{E_A}{kT}} \tag{11}$$

where E_A is the activation energy needed to overcome the barrier surrounding defects.

If we consider now that the effective bandgap both in the QW and said barrier are subject to polarisation fields and the QCSE, free-carrier screening of the field leads to a reduction of the barrier height (linear approximation)

$$E_A = E_A^0 - an \tag{12}$$

since both reduced well width and lower In content (in the barriers surrounding dislocations) lead to a smaller QCSE and therefore to a smaller screening-induced shift of the bandgap. Therefore we can now write

$$\tau_{nr} = \tau_{nr}^0 \exp^{\frac{E_A^0}{kT}} \exp^{-\frac{an}{kT}} \tag{13}$$

showing that the effective nonradiative lifetime is reduced at higher carrier density.

As mentioned earlier, we have neglected the effect of screening on the exciton oscillator strength, i.e. the exciton radiative lifetime. By calculating the emission energy and oscillator strength as a function of the field for the parameters of the QW of Fig. 7 and comparing the results with the experimentally observed peak shift with excitation power, we find that the oscillator strength increases with power by about 20 %. On the other hand, the decrease of nonradiative lifetime estimated from eq. 13 and the same peak shift depends on temperature: While τ_{nr} decreases by about a factor of 600 at 15 K, the change is only about 30 % at room temperature. Of course, the absolute values differ strongly between low temperature and room temperature. Nevertheless, it is clear that while the screening-induced change of the radiative part is independent of temperature, the change of the nonradiative part depends strongly on temperature.

In fact, performing the analysis using the full model leads to very satisfactory results. As shown by the fit curves in Fig. 7, the experimentally observed behaviour can be nicely reproduced by the model. Moreover, even the variation with temperature comes out correctly, as the drop in efficiency is most pronounced at the lowest temperature and is reduced towards higher temperature.

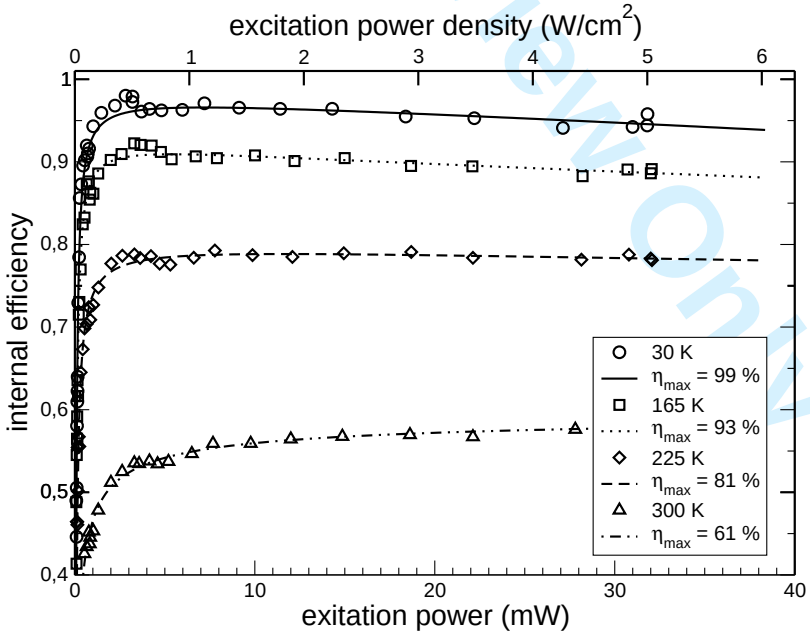

Figure 7. Excitation power dependence of the internal quantum efficiency of a 2 nm GaInN/GaN DQW sample ($\lambda_{em} \approx 460$ nm), plotted on a linear scale. At low temperature, a clear drop in efficiency at higher excitation power density is observed. For the model see text.

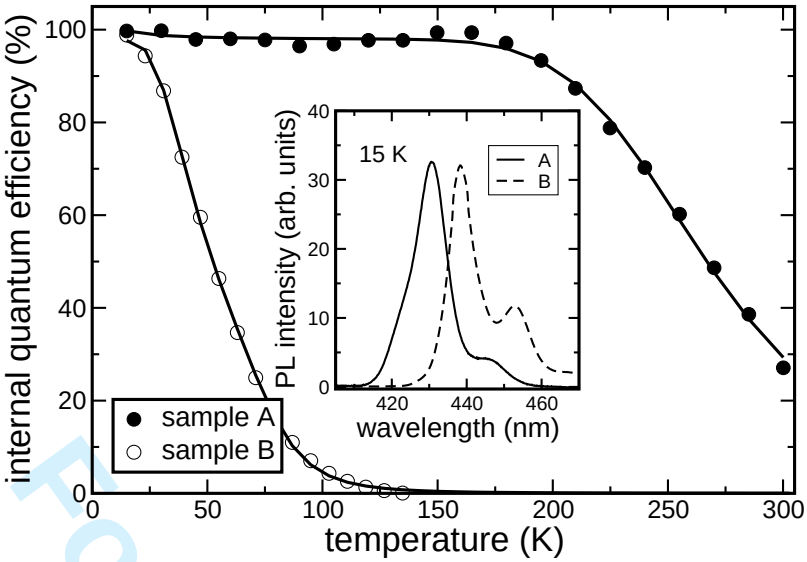

Figure 8. Temperature-dependent internal quantum efficiency of two typical samples investigated with the near-field microscope (excitation power density *approx* 10 W/cm^2). The inset shows low-temperature photoluminescence spectra.

4 Spatially resolved luminescence

In order to reveal the mechanism prohibiting nonradiative recombination of mobile free excitons with little or no localisation, we have used highly resolved spectroscopic near-field microscopy both at room temperature and at low temperature. Results from such measurements are expected to provide insight into the local potential profile present in the samples.

In the following we will specifically discuss data obtained for two samples, which have similar emission wavelengths of 430 nm (sample A, double QW) and 440 nm (sample B, single QW) but differ strongly in their room temperature (RT) internal quantum efficiency. As shown in Fig. 8, sample A reaches an internal efficiency of about 30 % at RT, while sample B hardly emits any light at RT, i.e. has a quantum efficiency below 10^{-3}. Still, the two samples exhibit quite comparable photoluminescence intensities at low temperature.

Looking at the two samples with the SNOM and focusing on the spectrally integrated low-temperature (20 K) emission intensity as in Fig. 9, we note that strong local intensity variations occur in both samples. The characteristic length scale of the intensity variations is of the order a few hundred nanometers in both cases. The typical density of threading dislocations is about 10^9cm^{-2} in these samples, i.e. the typical average distance of dislocations is about 300 nm. Sample C in Fig. 10 has dislocations decorated and was imaged using a dedicated atomic force microscope (AFM). The smoothed AFM image shows that the observed intensity pattern in the SNOM images is obviously correlated with the dislocation structure. Unfortunately, the topography information available from the near-field microscope does not allow us to resolve the position of single dislocations.

Nevertheless, as far as the spectrally integrated intensity distribution is concerned, we may conclude that the two sample exhibit a similar behaviour.

The situation becomes different when looking at single-wavelength images, also taken at low temperature. While such images taken at wavelengths close to the peak of the main QW emission are very similar to the integrated images shown in Fig. 9, images for wavelengths in the range 380 - 410 nm taken for sample A are vastly different: Nanometer-sized bright spots appear which change quickly at different wavelength. Fig. 11a shows three such images at wavelengths of 385 nm, 400 nm, and 409 nm combined using a colour-coding scheme. Pure red, green, or blue spots in this image indicate dominant emission at one particular wavelength from this spot. Mixed colours (additive colour mixing) indicate contributions from several wavelengths. The typical diameter of those spots is of the order 100 - 200 nm, most likely limited by the resolution of the near-field probe used in this particular measurement.

In Fig. 11b we show local spectra, each taken at one of the respective bright spots and plotted using the

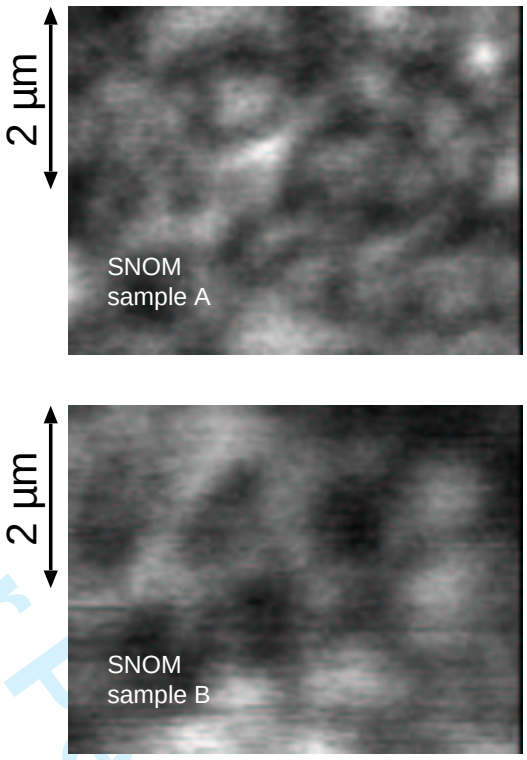

Figure 9. Spectrally integrated low-temperature near-field images of samples A and B covering a 5 x 3.8 μm area with 128 x 98 scan points.

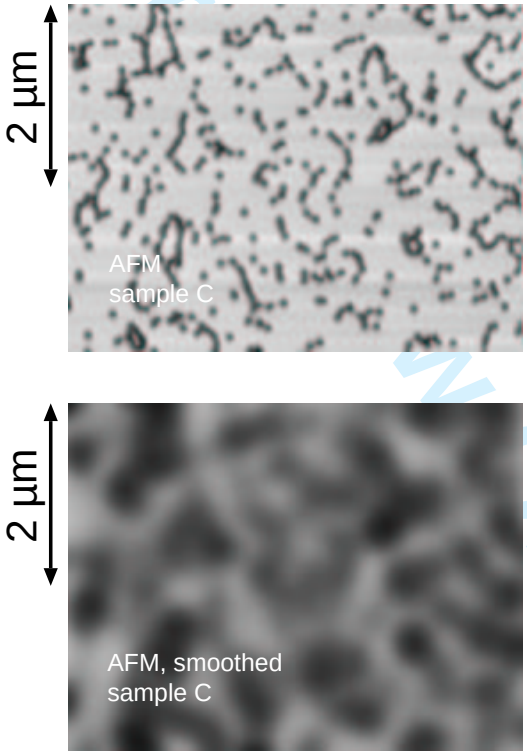

Figure 10. AFM image of a (different) sample C with dislocations marked shows the typical dislocation structure (top). The smoothed image (bottom) simulating the finite resolution of the SNOM shows a spatial structure very similar to the SNOM images of Fig. 9.

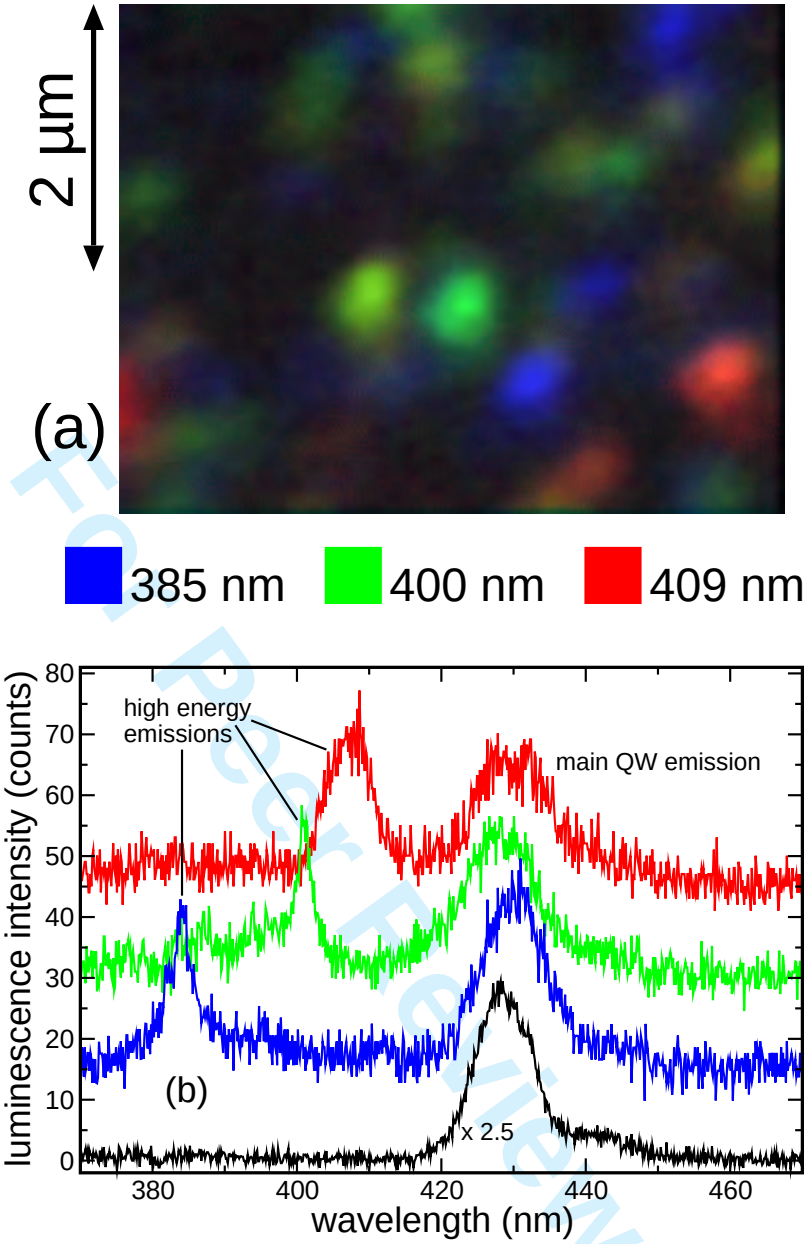

Figure 11. Combined near-field image of selected emissions at short wavelength (a) and corresponding local spectra (b) from sample A. As the signal from regions emitting at the main 430 nm line (lowest spectrum) is much stronger than the short-wavelength emission, there is always some crosstalk of the 430 nm emission.

same colour-coding. We observe narrow emission lines, with spectral widths down to 2 nm, in addition to the main QW emission at 430 nm. The local spectra are an individual fingerprint of each of the bright spots in Fig. 11a, which show that additional emissions occur in the wavelength range 380 - 410 nm. Each of the local spectra exhibiting the short-wavelength emissions also shows a contribution of the main 430 nm emission, although at much lower intensity compared to areas where the main emission is bright. This is a likely consequence of the finite spatial resolution, which mixes emissions from areas emitting at short-wavelength and those emitting at the main 430 nm peak.

All attempts to find similar short-wavelength emissions from sample B produced negative results: For sample B we find no structure in the near-field images taken at wavelengths shorter than the main emission. Given our sensitivity and noise level we can say that short-wavelength contributions from sample B are at least one order of magnitude weaker than those observed from sample A. On the other hand, other high-efficiency samples like sample A always exhibited such short-wavelength emissions, not all of which are as bright as observed for sample A discussed here.

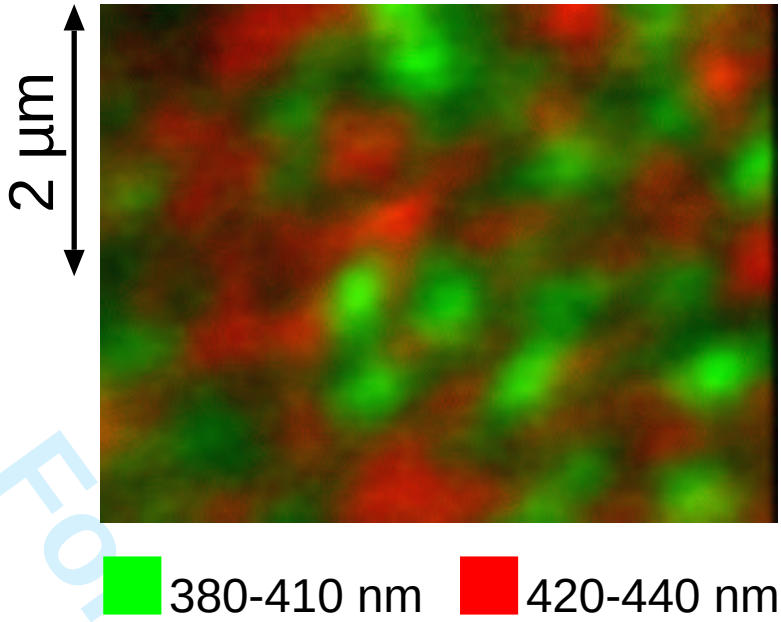

Figure 12. Combined near-field image of the integrated short-wavelength range (green) and the long-wavelength range (red). True complementarity is observed.

In order to understand the origin of the short-wavelength, high-energy emissions we take two images, one integrating the short-wavelength part of the spectra (380 - 410 nm), the other integrating the longer-wavelength part of the spectra (420 - 440 nm). In Fig. 12 we again use a colour-coding procedure, where the longer-wavelength image is in red and the shorter-wavelength image is in green, both combined using additive colour mixing.

Most importantly, we note that the two contributions are truly complementarity, i.e. regions strongly emitting at the main 430 nm line are dim in the short-wavelength image and vice versa. This is immediately visible from the lack of yellowish regions in Fig. 12, as a mixture of of red and green would produce yellow. This means that regions emitting at high energy do not significantly contribute to the main emission.

Moreover, we also see from Fig. 12 that there are essentially no dark regions, i.e. at any position in the image area there is either emission on the main 430 nm line or in the high-energy range. One would expect defects to produce dark areas for the main emission, but obviously all those areas dark in the main emission do emit in the high-energy range. Thus we must conclude that the high-energy emissions come from regions close to the defects. If in turn all regions close to defects emit at higher energy, those regions must have a higher bandgap than the normal quantum wells "far" from the defects.

Based on these observations, an interesting novel picture explaining the high emission efficiency of such samples emerges: If defects are surrounded by regions exhibiting a bandgap larger than that of the "normal" QW's, then carriers at energies around the "normal" bandgap (i.e. 430 nm in the present case) need to overcome an energy barrier in order to move towards the defects and to recombine nonradiatively. If the difference in bandgap is large enough (300 - 400 meV in the present case) the thermal energy of carriers even at room temperature will not be sufficient to allow them reaching the defects.

It is interesting to consider the possible origin of the high-bandgap regions. In quantum well structures, a larger bandgap can be the consequence of i) reduced In incorporation, ii) reduced well with, or iii) reduced strain or polarisation field. For the high-efficiency samples investigated in this study, it seems that one of these mechanisms takes place in the vicinity of threading dislocations. In fact, Duxbury *et al.* [34] have observed reduced In content close to dislocations in GaInN multiple quantum wells.

On the other hand, no evidence for high-bandgap regions was found for low-efficiency samples. Rather than that, dark areas with no emission are observed for such samples. As the nucleation and buffer layers of the samples are nominally identical, very similar defect densities are expected. Thus we conclude that in case of low-efficiency samples, no high-bandgap regions are generated during growth such that dislocations remain active recombination centres.

5 Microscopic structure

Cross-sectional transmission electron microscopy reveals quantum wells with highly perfect interfaces. Fig. 13 shows a single QW structure with low room-temperature photoluminescence efficiency, as in case of sample B used in the near-field studies (c.f. Fig. 8 and 9). Even in the immediate vicinity of threading dislocations, the QW remains flat and regular.

On the other hand, transmission electron microscopy of optimised QW structures shows that again highly perfect interfaces are obtained for c-plane QW's. A TEM image of a typical multiple quantum well (MQW) structure of this kind is shown in Fig. 14. In this case, the QW's have a thickness of 3.5 nm and a period of 11 nm on the (0001) plane. However, in the vicinity of a threading dislocation the QW's clearly follow a V-shaped pit. Inside the pit, the quantum wells grown on the $(1\bar{1}01)$ sidewalls exhibit a much smaller thickness. Moreover, the barrier between the QW's on the sidewalls of the pit is also much thinner than in case of the c-plane QW's. This is also shown schematically in Fig. 14b.

For this structure we find a QW spacing of 2.3 nm on the $(1\bar{1}01)$ sidewalls, compared to 11 nm on the (0001) plane. The QW width is determined to approximately 1.1 nm on the sidewalls of the pit compared

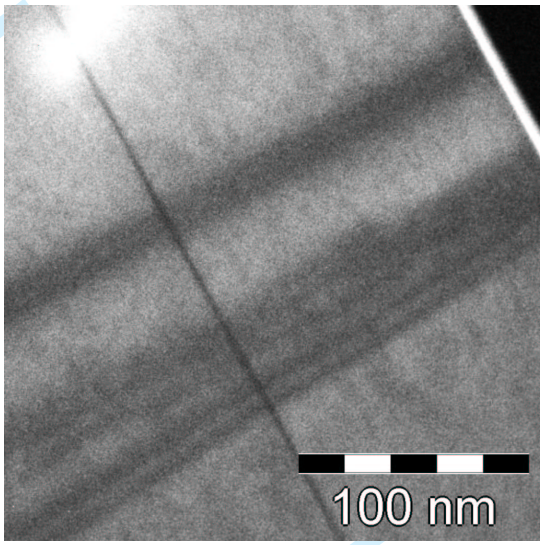

Figure 13. Transmission electron microscope image of a GaInN/GaN single quantum well structure with low emission efficiency. Even in the vicinity of a threading dislocation, the interfaces remain flat and parallel to the c-plane.

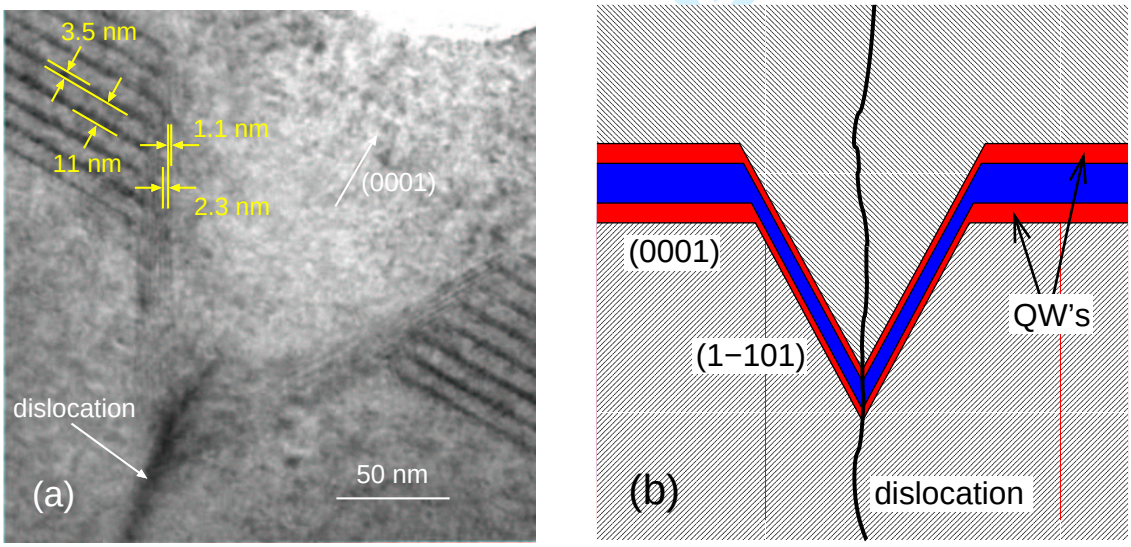

Figure 14. Transmission electron microscope image (a) of a GaInN/GaN multiple quantum well structure. In the planar region high quality QW's with well-defined sharp interfaces are visible. In the vicinity of a threading dislocation, a V-shaped pit appears with sidewall QW's with a thickness and spacing much lower than for the (0001) QW's. This is also schematically shown in (b).

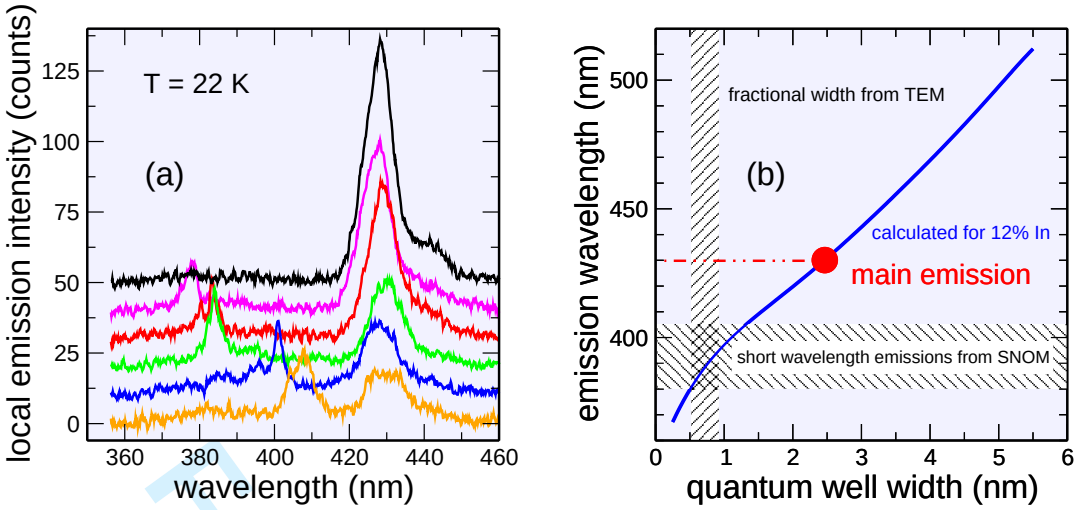

Figure 15. Comparison of TEM and near-field PL data: (a) shows low-temperature emission spectra obtained from nm-size areas close to threading dislocations with a near field microscope [37]. Besides the main emission at 430 nm multiple sharp peaks from different locations appear in the range 380 - 410 nm. Utilizing the calculated emission wavelength vs. QW width we compare the c-plane QW and the sidewall QW widths (reduction ratio from Fig. 14) with the main emission and the short wavelength emissions observed in SNOM measurements.

to 3.5 nm on the (0001) plane. On the other hand, considering that the growth of the barriers and of the QW's is under identical conditions except for the In incorporation, we expect the QW thickness to scale the same way as the QW spacing. Consequently, for the 3.5 nm c-plane QW in Fig. 14 the associated thickness of the sidewall QW's would be only about 0.7 nm, somewhat less than the 1.1 nm determined directly. Given the uncertainties in both methods to determine the QW width together with fluctuations between different pits, we use 0.9 ± 0.3 nm as the reduced QW width.

It is interesting to note that in a simple-minded geometric view one would expect the growth rate on the facets to scale as the cosine of the angle, giving a ratio of 0.47 between the $(1\bar{1}01)$ and the (0001) planes. The experimental value is around 0.25 showing that growth on the $(1\bar{1}01)$ facet is much slower than on the c-plane under the conditions used. This explains why pits develop at all and tend to get larger with increasing layer thickness.

Now, if the sidewall QW's are that much thinner than the c-plane QW's, quantum confinement together with a reduced QCSE would lead to a considerably larger bandgap of the sidewall QW's. In Fig. 15 we compare the reduction of thickness obtained from the present TEM data to the change in emission energy obtained from the near-field data. Fig. 15a shows low-temperature emission spectra obtained from different nm-sized areas of a (different) sample with two 2.5 nm GaInN QW's. While spectra obtained between defects (black) exhibit only the 430 nm main QW emission, spectra from areas close to defects show additional emission peaks in the 380 - 410 nm range.

In order to compare the SNOM data with the TEM results, we use the calculated dependence of emission wavelength on well thickness, as shown in Fig. 15b. The calculation is based on solving Schrödingers equation for a quantum well with a built-in field, and utilises the experimentally obtained bandgap of GaInN [35] as well as the polarisation field [12] as a function of In content. In addition the field on the $(1\bar{1}01)$ plane should be lower than on the (0001) plane for symmetry reasons, but this will have only a minor effect for such thin quantum wells. Clearly, the reduced QW thickness in the sidewall QW leads to an emission wavelength well within the range observed for the high-energy emission in the near-field measurements. In fact, from experiments with QW's grown on faceted laterally-overgrown GaN/SiC structures we know that inclined QW's on $(1\bar{1}01)$ facets do exhibit much shorter wavelength emission [36].

The presence of V-shaped pits and of thin sidewall QW's is clearly associated with high internal efficiency. In fact, the TEM images (Fig. 16) together with atomic force microscope (AFM) images of un-capped samples suggest that practically every defect is decorated with such a pit. Moreover, we observe a reduced thickness of the sidewall QW's not only for rather thick QW's (as in Fig. 14, where the effect is seen most clearly in the TEM image) but also for QW's with thicknesses below 2 nm, which exhibit the highest internal efficiencies. On the other hand, non-optimised samples exhibiting fairly low room temperature

efficiency but good low temperature PL reveal no evidence for such pits and sidewall QW's (c.f. Fig. 13).

Based on these observations we propose that suppression of nonradiative recombination in high efficiency GaInN/GaN quantum wells is due to a self-screening of the defects. The formation of V-shaped pits leads to narrow sidewall quantum wells surrounding every defect, with an effective bandgap several hundred meV higher than that of the "normal" c-plane QW's. Thus an energy landscape as visualised in Fig. 17 emerges, where carriers are "anti-localised" rather than localised. A barrier height of the order 400 meV as obtained from the near-field data [37] is sufficient to suppress nonradiative recombination even at room temperature.

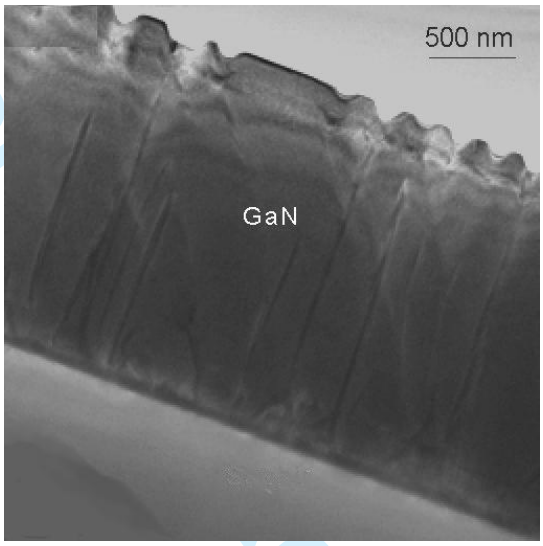

Figure 16. Low magnification TEM image of the GaInN/GaN multiple quantum well structure from Fig. 14. Every dislocation throughout the image is terminated by a V-shaped pit.

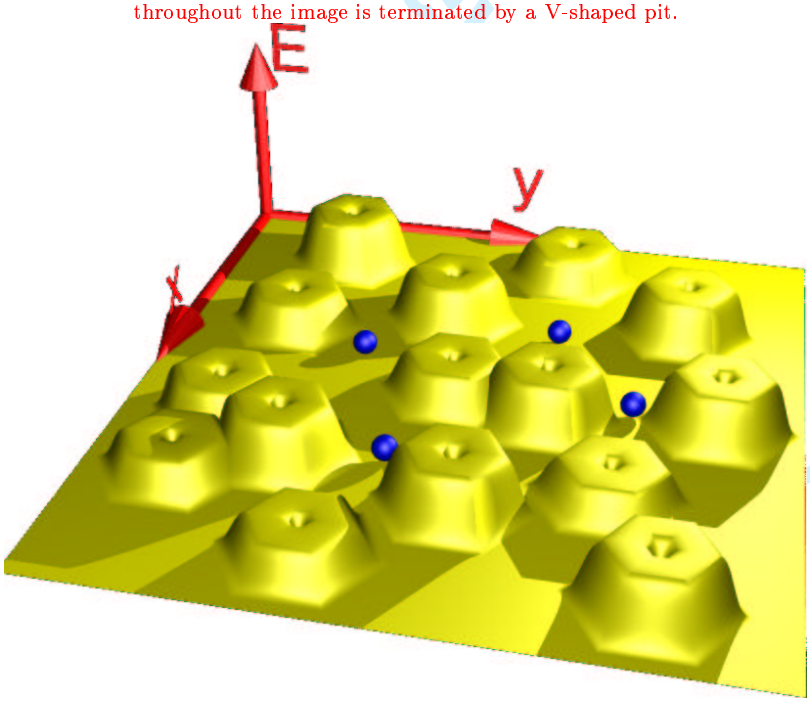

Figure 17. Visualisation of the energy landscape resulting from V-shaped hexagonal pits exhibiting increased bandgap in the sidewalls. Carriers in the regular c-plane QW's (with lower bandgap) in between have to overcome a large energy barrier to reach the defects and to recombine nonradiatively.

6 Discussion

The analysis of both the temperature dependence and the excitation power dependence of the internal efficiency discussed in the previous sections reveals several important insights:

(i) Localisation of excitons is inconsistent with an efficiency decreasing towards low excitation power density even at low temperature. We can therefore exclude that localisation is the primary reason for low nonradiative recombination and high room-temperature efficiency in our high-quality QW's. At low temperature, exciton localisation may still be of some importance.
(ii) Free excitons play a major role for the emission efficiency. In the temperature dependence, their binding energy appears as an activation energy. In the excitation power dependence, the mass-action-law between excitons and free carriers governs the quantitative behaviour of the efficiency.
(iii) Separate localisation of electrons and holes reduces the free exciton concentration and thus the emission efficiency at low excitation power densities and low temperatures.
(iv) Carrier confinement in the QW is a limiting factor for the efficiency.

From these observations it becomes clear that **carriers are mobile** at room temperature even in the most efficient GaInN/GaN quantum well structures. This is clearly evident from the increase of efficiency with increasing excitation power and carrier density, due to increasing formation of **free excitons** from free electrons and holes. If excitons were localised, the highest efficiency should be observed at lower power density and a decrease of efficiency should be present at high carrier density, when filling and overflow of localised states occurs. On the contrary, the strong drop in efficiency at low power and low temperature evidences separate localisation of electrons and holes rather than exciton localisation, preventing them from efficient radiative recombination.

It is interesting to discuss these findings in the context of the recent literature. Recent data by Jahn *et al.* [38] obtained for GaInN/GaN QW's grown by MBE and MOVPE from cathodoluminescence measurements seem to indicate no drop in efficiency at low power levels, thus leading to the conclusion that indeed localisation dominates. Several reasons are possible for the discrepancy with our results: i) cathodoluminescence is *per se* non-resonant, i.e. excites all layers starting from the surface and may thus be sensitive to transport and capture effects, ii) the samples studied in Ref. [38] exhibit a room-temperature efficiency of at most 1 % and may thus be subject to different mechanisms (our samples exhibited a room-temperature efficiency of up to 73 %).

As to the microscopic mechanism, mother nature obviously provides a fascinating way prohibiting nonradiative recombination: The narrow sidewall quantum wells in V-shaped pits represent energy barriers keeping carriers away from dislocations. While V-shaped pits have so far been looked at as "defects" [20–22], which should be avoided, their highly beneficial role suppressing nonradiative recombination makes control of these structural entities highly desirable.

It is interesting to note that to our knowledge so far no V-shaped pits have been reported for nitride QW's grown by molecular beam epitaxy (MBE). This may explain the common observation that MBE-grown GaInN-based LED's exhibit considerably lower efficiency than comparable MOVPE-grown devices, as there would be no self-screening of the defects in the MBE case.

Provided that binding into free excitons indeed increases the internal efficiency, design rules for optimum emission efficiency emerge: i) the QW width should be less than about 2.5 nm to avoid a reduced oscillator strength induced by the QCSE, ii) for the maximum excitonic effect, the QW width should be designed to give the highest exciton binding energy (about 2 nm), iii) background electrons (from n-type doping of the barriers and/or the underlying layer of the QW's) stabilise excitons (since $x \propto (\delta n + n_0) \cdot \delta p$) and thus give a higher radiative recombination probability, iv) barriers around the QW's should be high enough to give sufficient carrier confinement in the wells.

On the other hand, optimisation of QW's for high efficiency involves generating barriers around every defect. By maximising the height of the barriers (i.e. minimal thickness of the sidewall QW's) nonradiative recombination can be minimised. Doing this one should keep in mind that the total fractional area of the pits should be as small as possible to maximise the area of the c-plane QW's emitting light at the design wavelength.

7 Conclusion

In conclusion, we have studied the structural properties and their correlation with the internal quantum efficiency of high-performance GaInN/GaN quantum wells emitting in the blue spectral region. From the temperature and excitation power dependence we conclude that besides carrier escape from the quantum well, binding into free excitons is governing the radiative recombination and thus is the key for high quantum efficiency. Localisation of excitons is not important at room temperature, according to our observations. On the contrary, separate localisation of electrons and holes at low temperature reduces the internal efficiency at low excitation levels.

Using a combination of growth optimisation, transmission electron microscopy, and scanning near-field optical microscopy we have obtained strong evidence that the unexpectedly high emission efficiency of GaInN-based quantum well light emitting diodes relies on self-screening of defects rather than random localisation. Hexagonal V-shaped pits decorating every threading dislocation can be forced to exhibit sidewall quantum wells with reduced thickness and higher bandgap thus leading to a potential barrier around every defect, which keeps carriers from recombining nonradiatively at the defect.

Therefore, instead of random localisation, anti-localisation by energy barriers around dislocations allows mobile free excitons to recombine radiatively and to provide the high light emission efficiency necessary for tomorrows light sources.

Acknowledgements

The authors gratefully acknowledge partial financial support of this work by the Deutsche Forschungsgemeinschaft (DFG).

References

[1] S. Nakamura, M. Senoh, N. Iwasa, and S.-I. Nagahama, Appl. Phys. Lett. **67**, 1868 (1995).
[2] S. D. Lester, F. A. Ponce, M. G. Craford, and D. A. Steigerwald, Appl. Phys. Lett. **66**, 1249 (1995).
[3] S. Nakamura, T. Mukai, and M. Senoh, Appl. Phys. Lett. **64**, 1687 (1994).
[4] S. Nakamura, M. Senoh, N. Iwasa, S.-I. Nagahama, T. Yamada, and T. Mukai, Jpn. J. Appl. Phys. **34**, L1332 (1995).
[5] S. Chichibu, T. Azuhata, T. Sota, and S. Nakamura, Appl. Phys. Lett. **69**, 4188 (1996).
[6] Y. Narukawa, Y. Kawakami, S. Fujita, S. Fujita, and S. Nakamura, Phys. Rev. B **55**, R1938 (1997).
[7] S. Nakamura, Science **281**, 956 (1998).
[8] K. P. O'Donnell, J. F. W. Mosselmans, R. W. Martin, S. Pereira, and M. E. White, J. Phys.: Condens. Matter **13**, 6977 (2001).
[9] Y. Narukawa, Y. Kawakami, M. Funato, S. Fujita, S. Fujita, and S. Nakamura, Appl. Phys. Lett. **70**, 981 (1997).
[10] T. M. Smeeton, M. J. Kappers, J. S. Barnard, M. E. Vickers, and C. J. Humphreys, Appl. Phys. Lett. **84**, 4110 (2004).
[11] F. Bernardini, V. Fiorentini, and D. Vanderbilt, Phys. Rev. B **56**, R10024 (1997).
[12] A. Hangleiter, F. Hitzel, S. Lahmann, and U. Rossow, Appl. Phys. Lett. **83**, 1169 (2003).
[13] E. E. Mendez, G. Bastard, L. L. Chang, L. Esaki, H. Morkoc, and R. Fischer, Phys. Rev. B **26**, R7101 (1982).
[14] T. Takeuchi, S. Sota, M. Katsuragawa, M. Komori, H. Takeuchi, H. Amano, and I. Akasaki, Jpn. J. Appl. Phys. **36**, L382 (1997).
[15] J. S. Im, H. Kollmer, J. Off, A. Sohmer, F. Scholz, and A. Hangleiter, Phys. Rev. B **57**, R9435 (1998).
[16] A. Hangleiter, J. S. Im, H. Kollmer, S. Heppel, J. Off, and F. Scholz, MRS Internet J. Nitride Semicond. Res. **3**, 15 (1998).
[17] A. Hangleiter, in *Low-Dimensional Nitride Semiconductors*, edited by B. Gil (Oxford University Press, Oxford, 2002), Chap. Optoelectronic devices based on low-dimensional nitride heterostructures.
[18] M. Gallart, P. Lefebvre, A. Morel, T. Taliercio, B. Gil, J. Allegre, H. Mathieu, B. Damilano, N. Grandjean, and J. Massies, phys. stat. sol. (a) **183**, 61 (2001).
[19] H. Amano, N. Sawaki, I. Akasaki, and Y. Toyoda, Appl. Phys. Lett. **48**, 353 (1986).
[20] F. Scholz, A. Sohmer, J. Off, V. Syganow, A. Drnen, J.-S. Im, A. Hangleiter, and H. Lakner, Mat. Sci. Eng. B **50**, 238 (1997).
[21] I.-H. Kim, H.-S. Park, Y.-J. Park, and T. Kim, Appl. Phys. Lett. **73**, 1634 (1998).
[22] Y. Chen, T. Takeuchi, H. Amano, I. Akasaki, N. Yamada, Y. Kaneko, and S. Y. Wang, Appl. Phys. Lett. **72**, 710 (1998).
[23] K. Hiramatsu, Y. Kawaguchi, M. Shimizu, N. Sawaki, T. Zheleva, R. F. Davis, H. Tsuda, W. Taki, N. Kuwano, and K. Oki, MRS Internet J. Nitride Semicond. Res. **2**, 6 (1997).
[24] D. Fuhrmann, C. Netzel, U. Rossow, A. Hangleiter, G. Ade, and P. Hinze, Appl. Phys. Lett. **88**, 071105 (2006).
[25] T. N. Morgan, Phys. Rev. B **28**, 7141 (1983).
[26] P. Michler, A. Hangleiter, M. Moser, M. Geiger, and F. Scholz, Phys. Rev. B. **46**, 7280 (1992).
[27] S. Lahmann, F. Hitzel, U. Rossow, and A. Hangleiter, phys. stat. sol. (c) **0**, 2202 (2003).
[28] S. Dhar, U. Jahn, O. Brandt, P. Waltereit, and K. H. Ploog, Appl. Phys. Lett. **81**, 673 (2002).
[29] B. Monemar, Phys. Rev. B **10**, 676 (1974).
[30] S. Kalliakos, X. B. Zhang, T. Taliercio, P. Lefebvre, B. Gil, N. Grandjean, B. Damilano, and J. Massies, Appl. Phys. Lett. **80**, 428 (2002).
[31] T. Mukai, M. Yamada, and S. Nakamura, Jpn. J. Appl. Phys. **38**, 3976 (1999).
[32] F. Hitzel, G. Klewer, S. Lahmann, U. Rossow, and A. Hangleiter, Phys. Rev. B **72**, 081309(R) (2005).
[33] A. Hangleiter, F. Hitzel, C. Netzel, D. Fuhrmann, U. Rossow, G. Ade, and P. Hinze, Phys. Rev. Lett. **95**, 127402 (2005).

[34] N. Duxbury, U. Bangert, P. Dawson, E. J. Thrush, W. V. der Stricht, K. Jacobs, and I. Moerman, Appl. Phys. Lett. **76**, 1600 (2000).
[35] J. Wu, W. Walukiewicz, K. M. Yu, J. W. A. III, E. E. Haller, H. Lu, and W. J. Schaff, Appl. Phys. Lett. **80**, 4741 (2002).
[36] F. Hitzel, U. Ahrend, N. Riedel, U. Rossow, and A. Hangleiter, phys. stat. sol. (c) **0**, 2674 (2003).
[37] F. Hitzel, G. Klewer, S. Lahmann, U. Rossow, and A. Hangleiter, phys. stat. sol. (c) **1**, 2520 (2004).
[38] U. Jahn, S. Dhar, O. Brandt, H. T. Grahn, and K. H. Ploog, J. Appl. Phys. **93**, 1048 (2003).

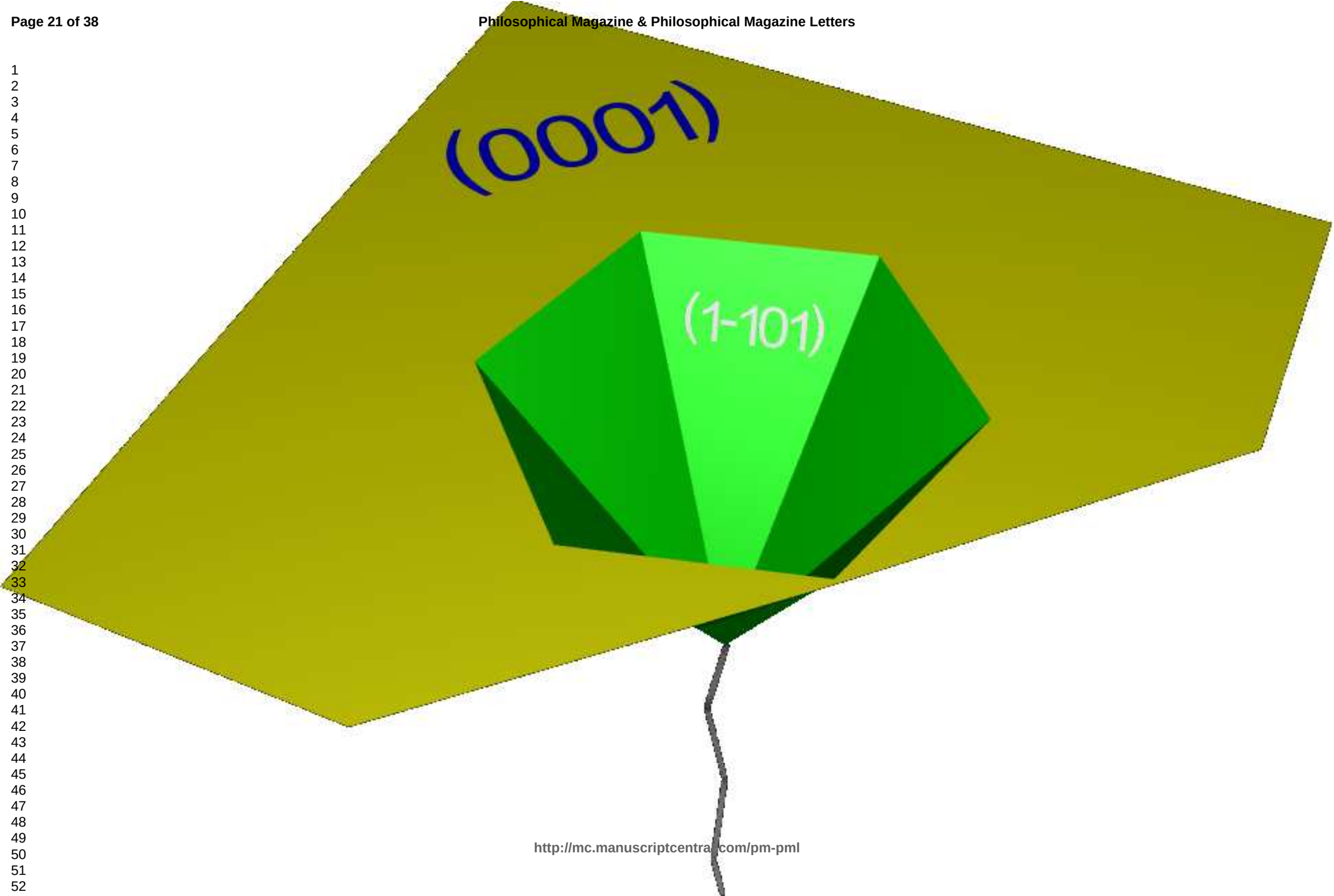
(0001)
(1-101)

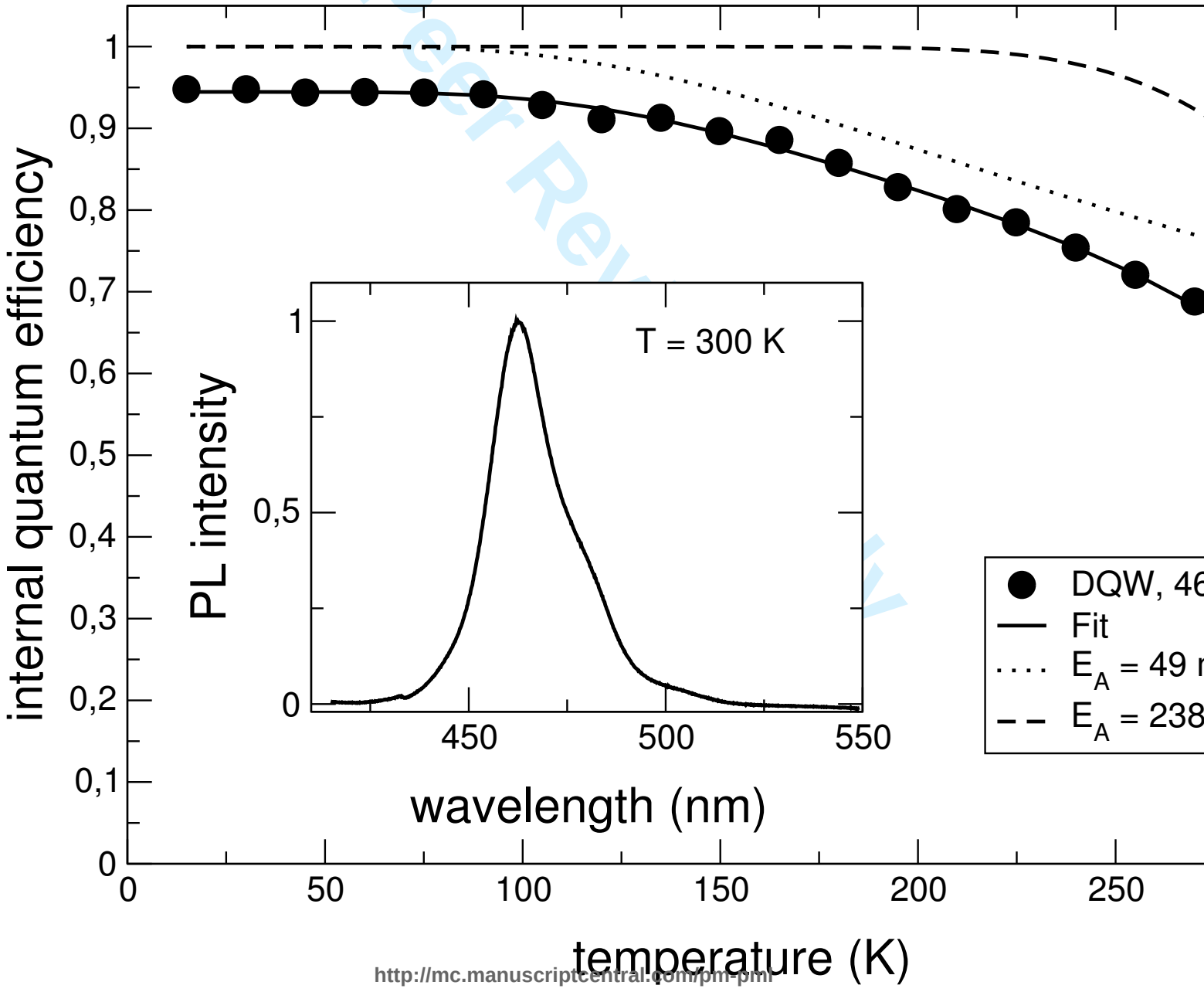

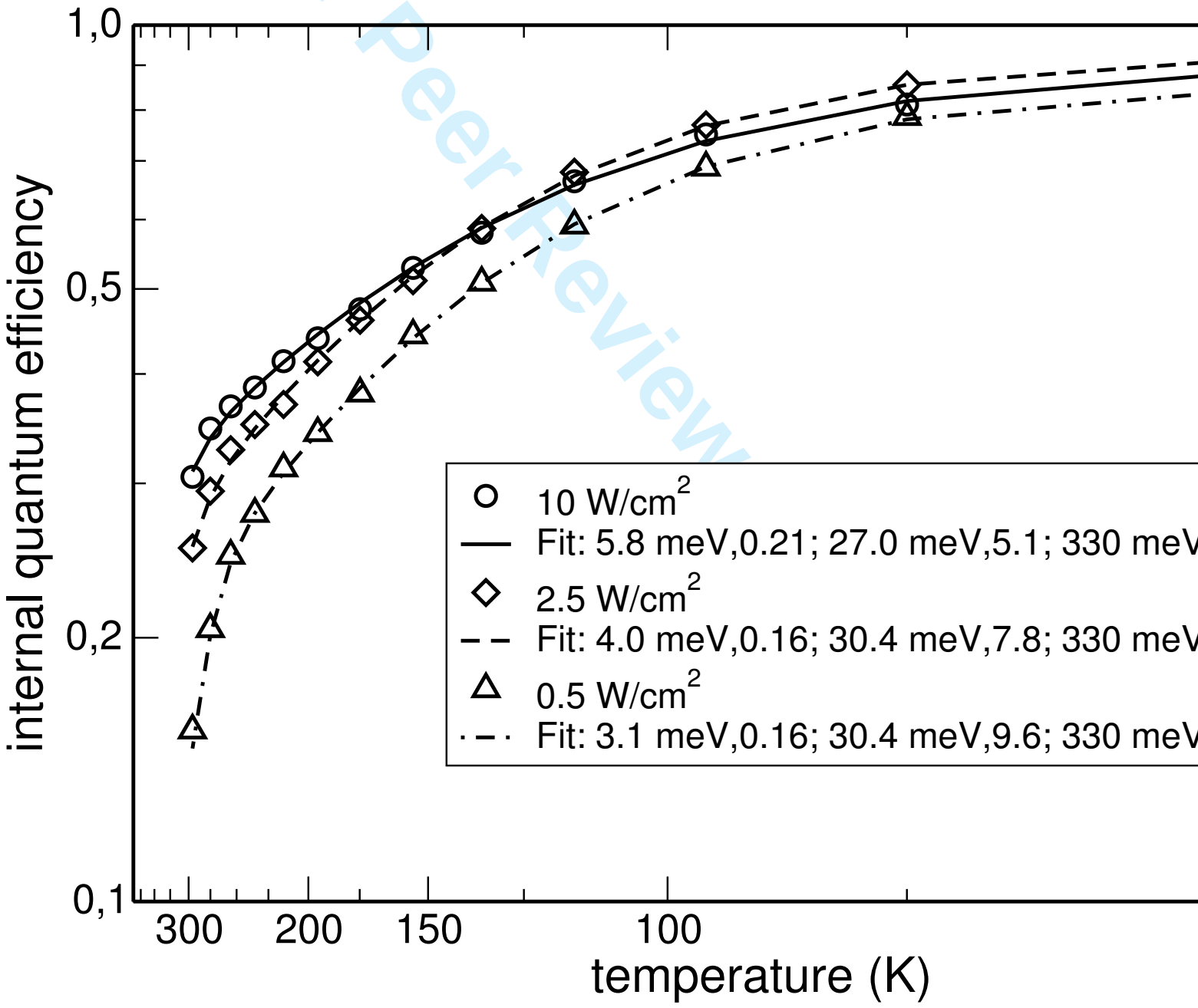

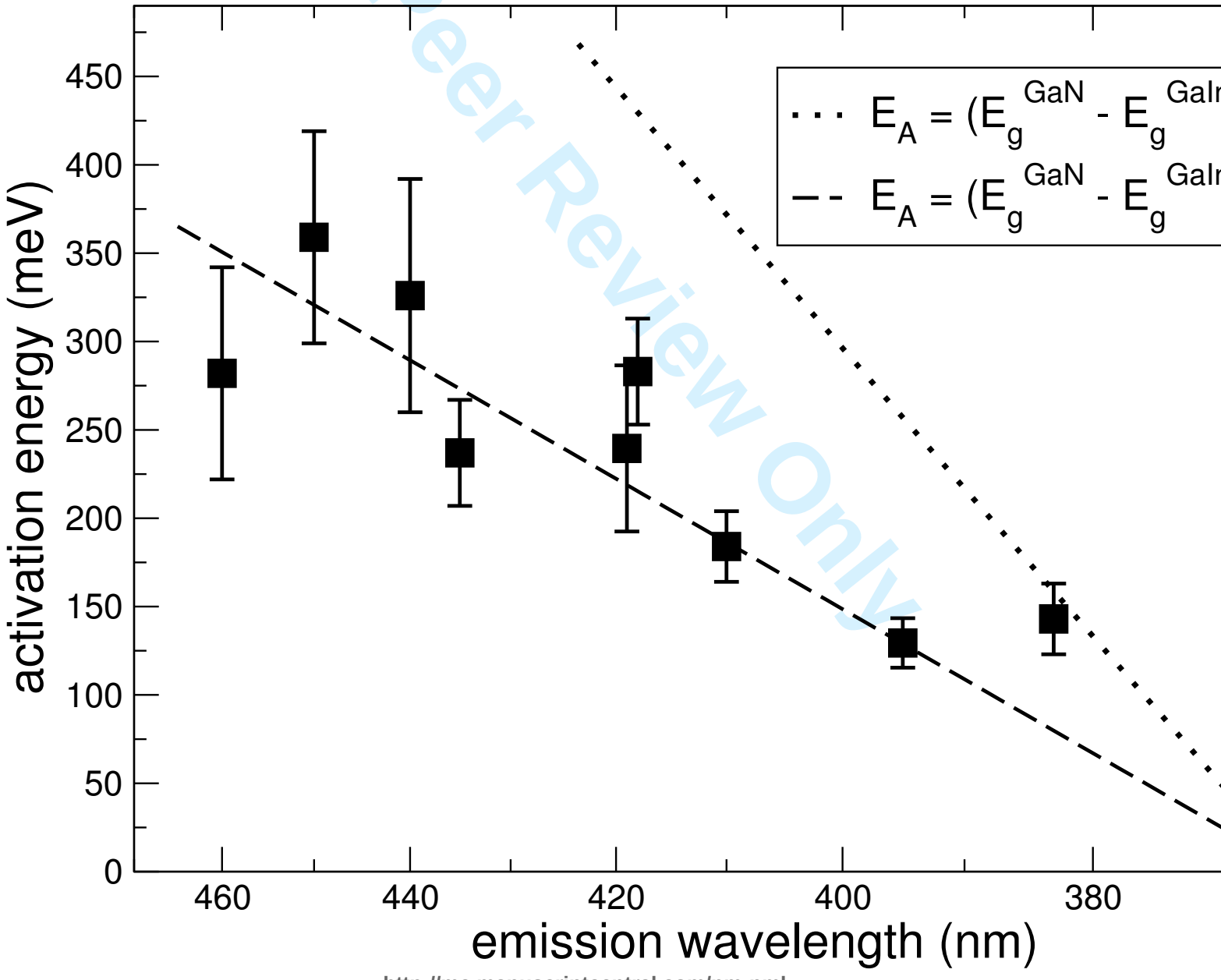

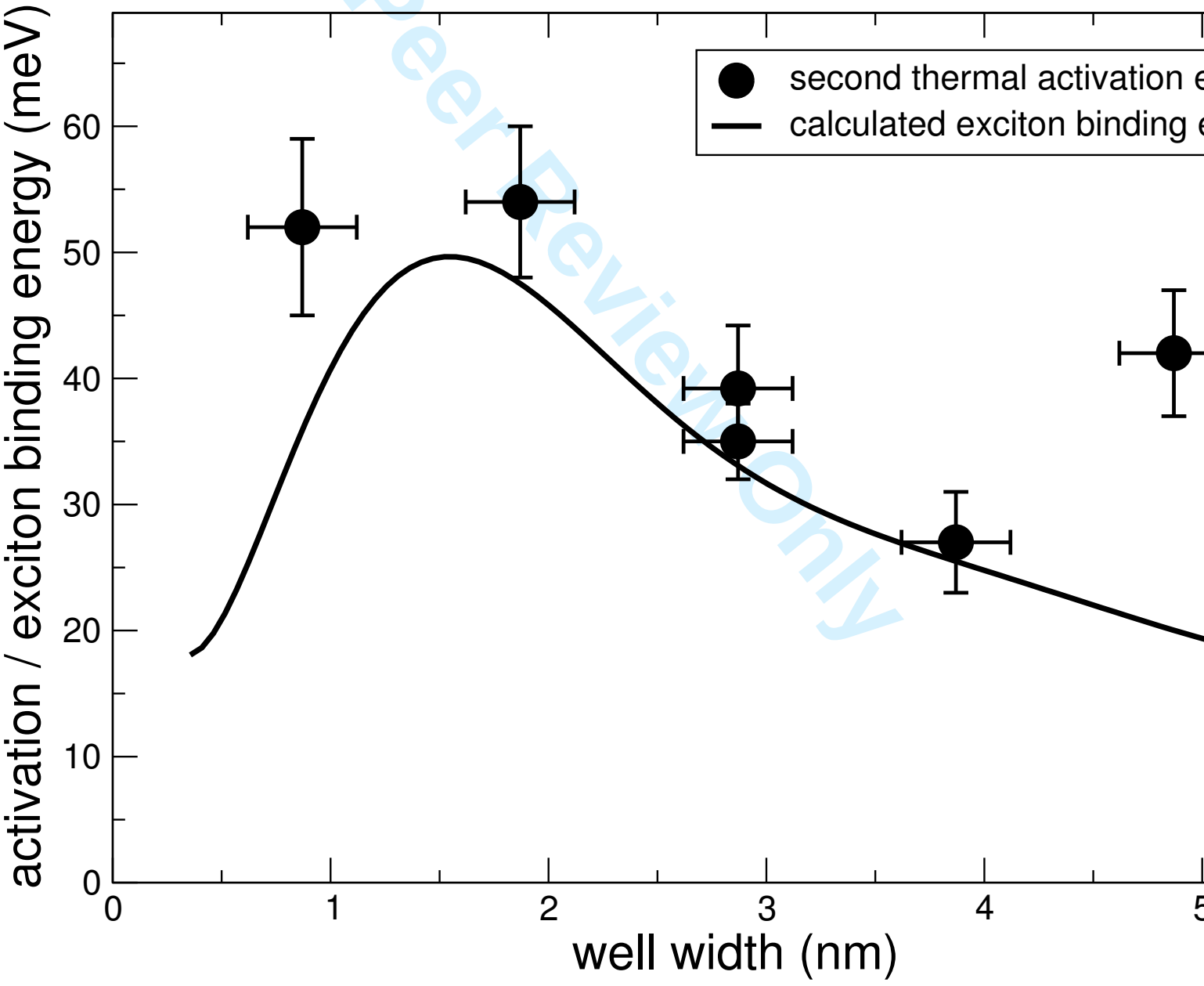

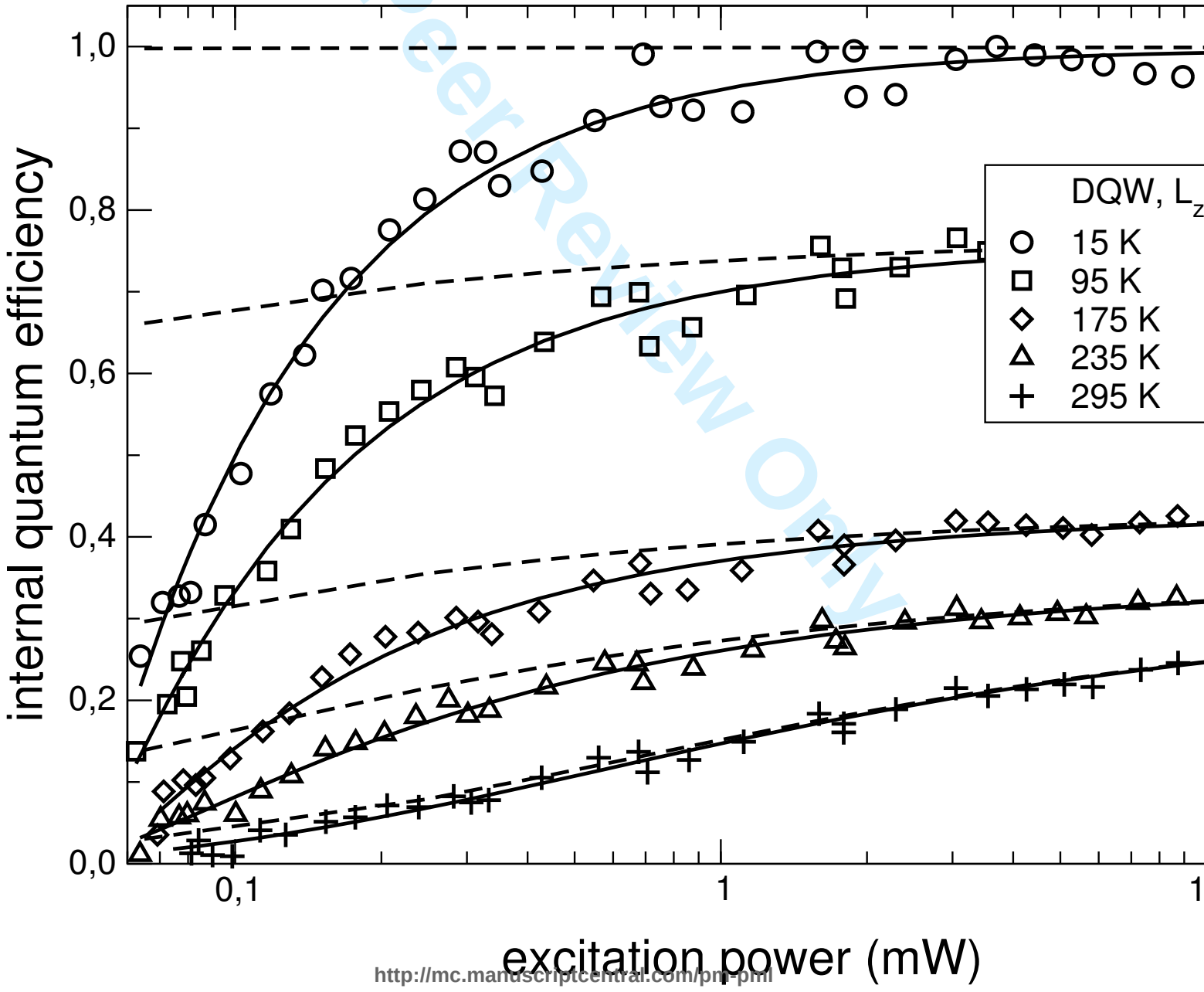

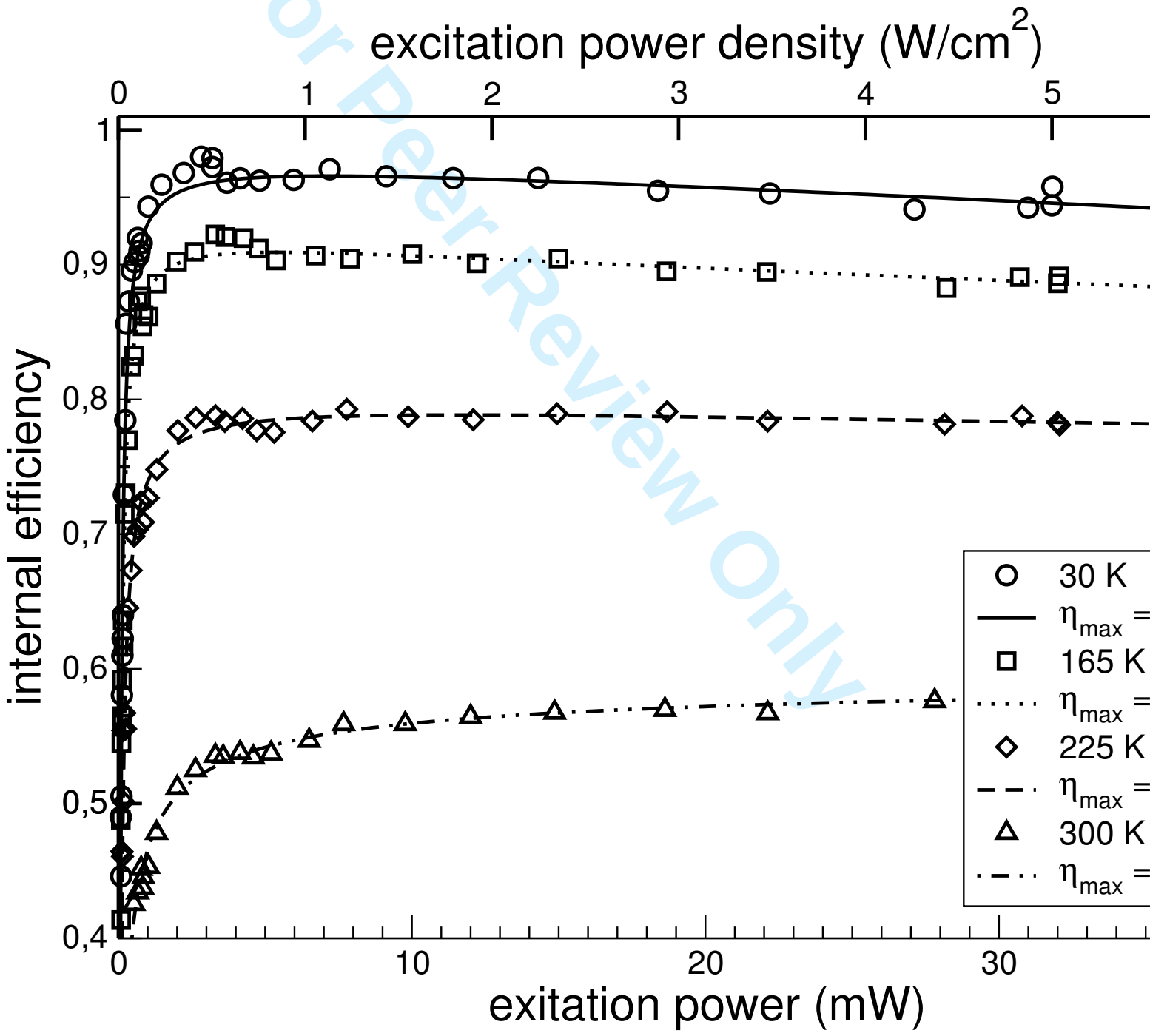

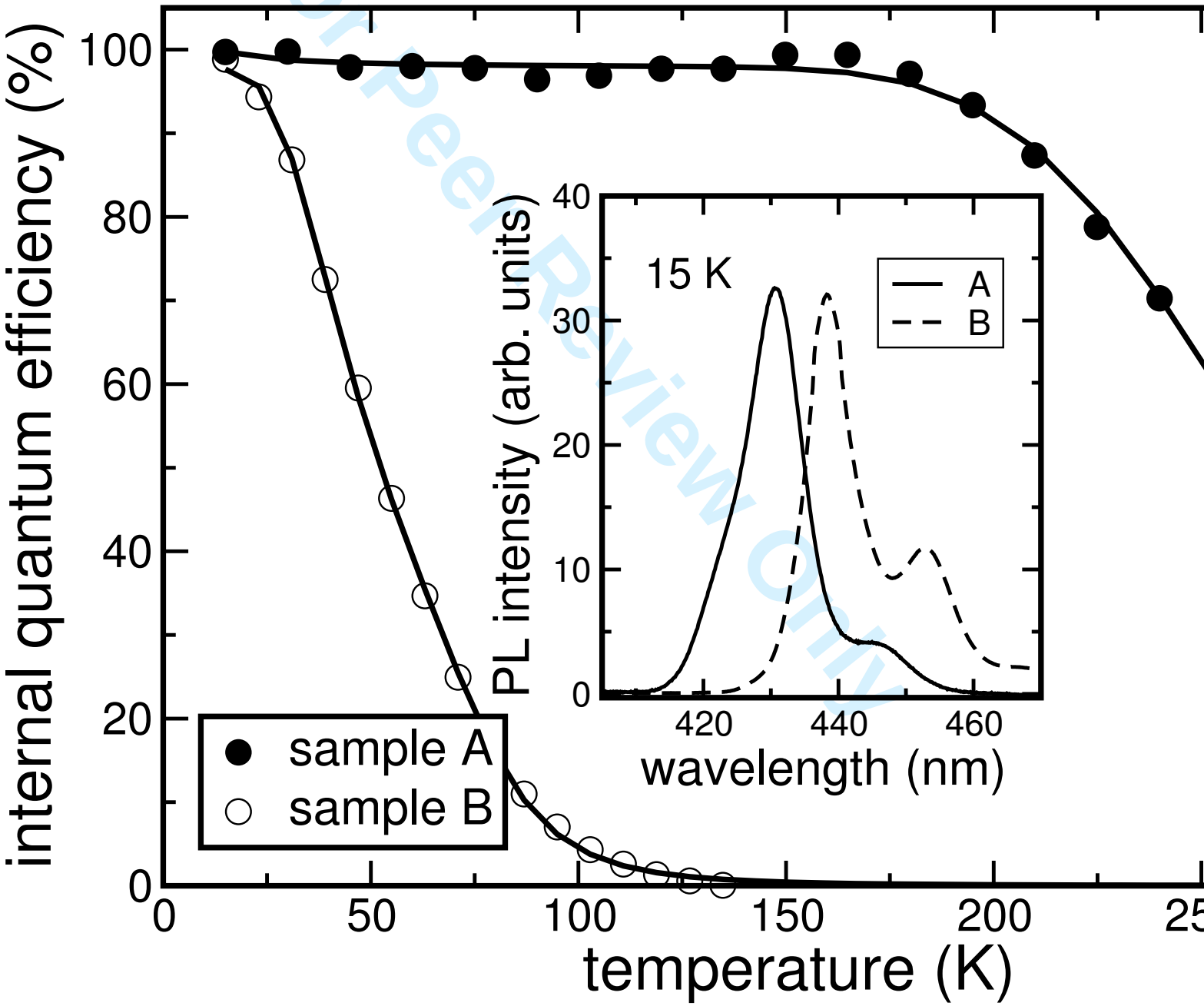

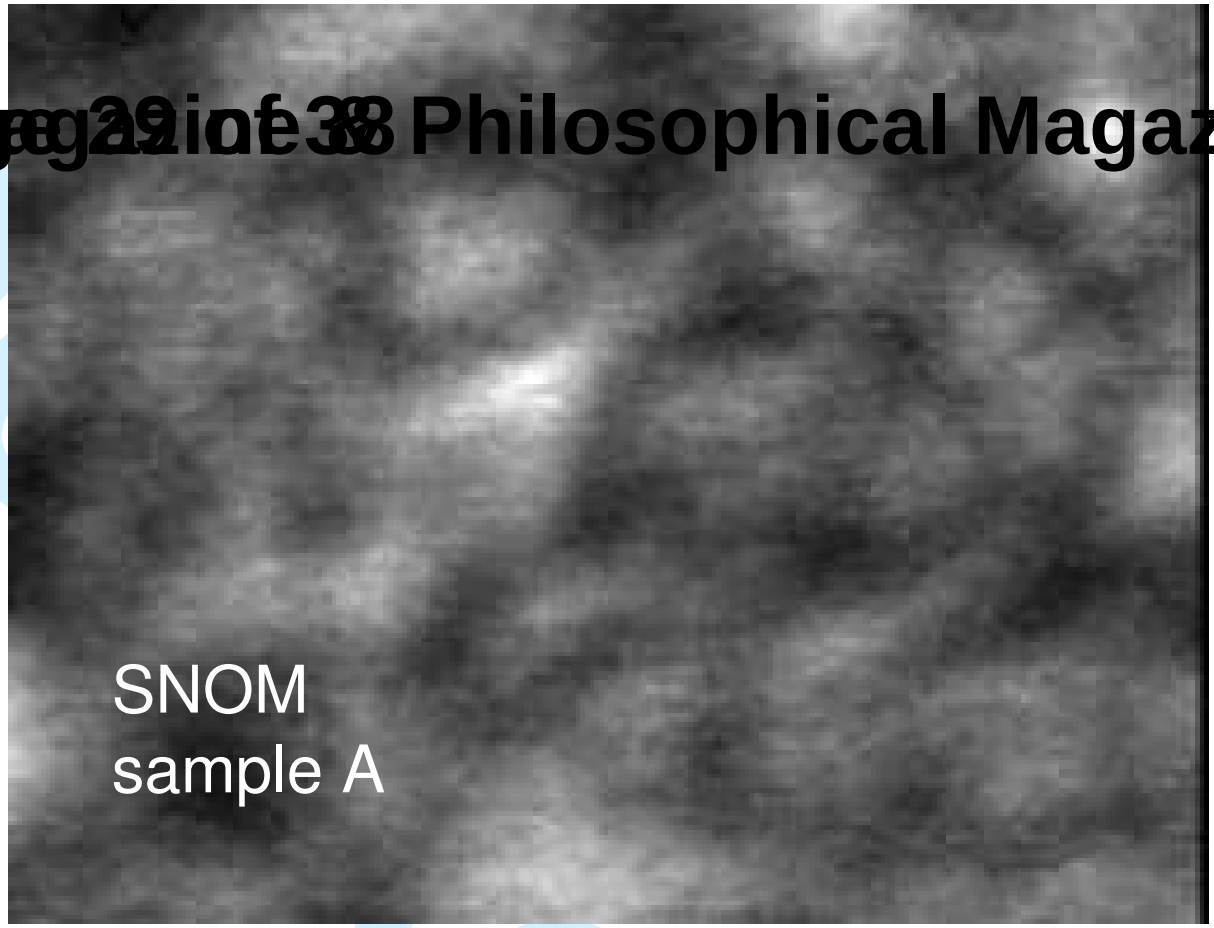

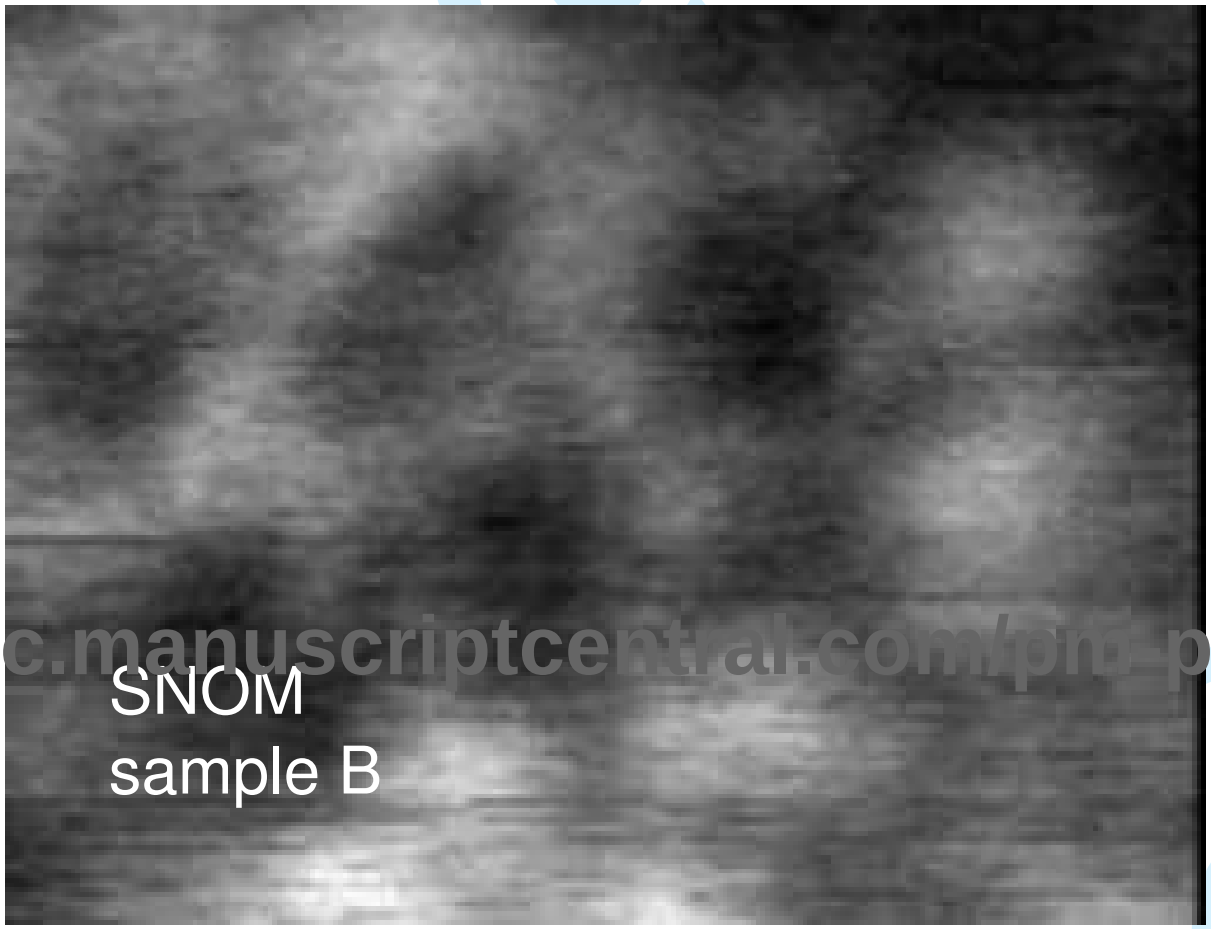

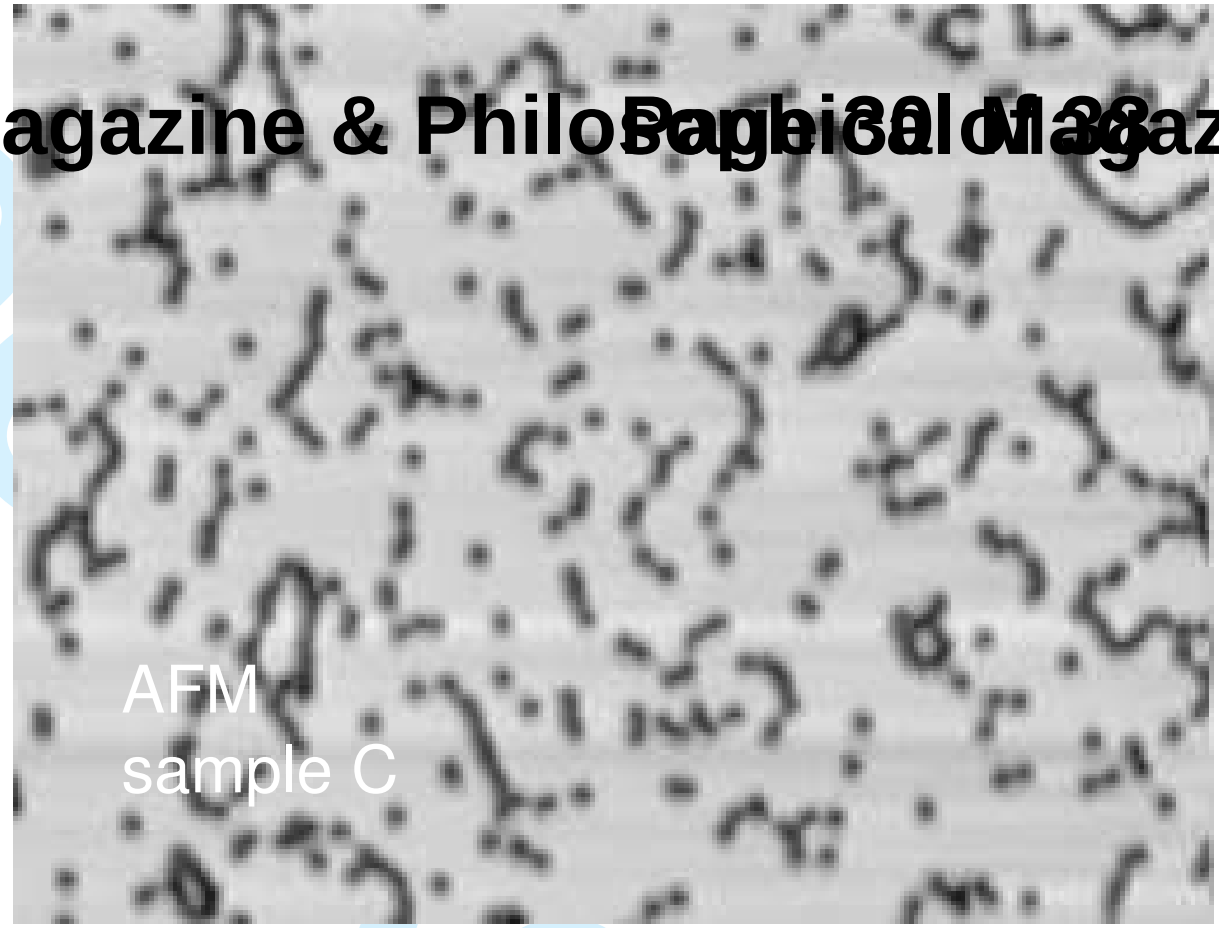

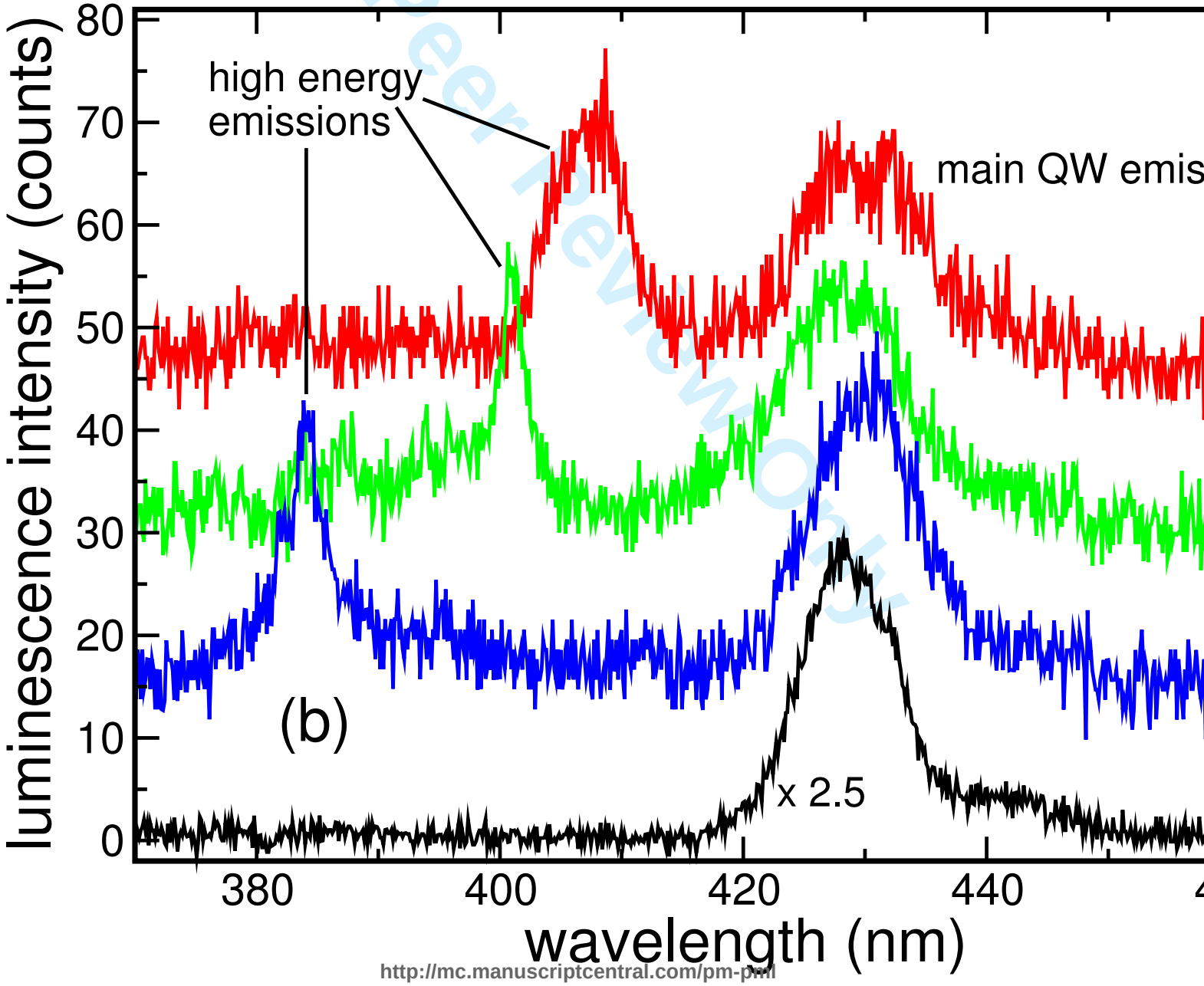

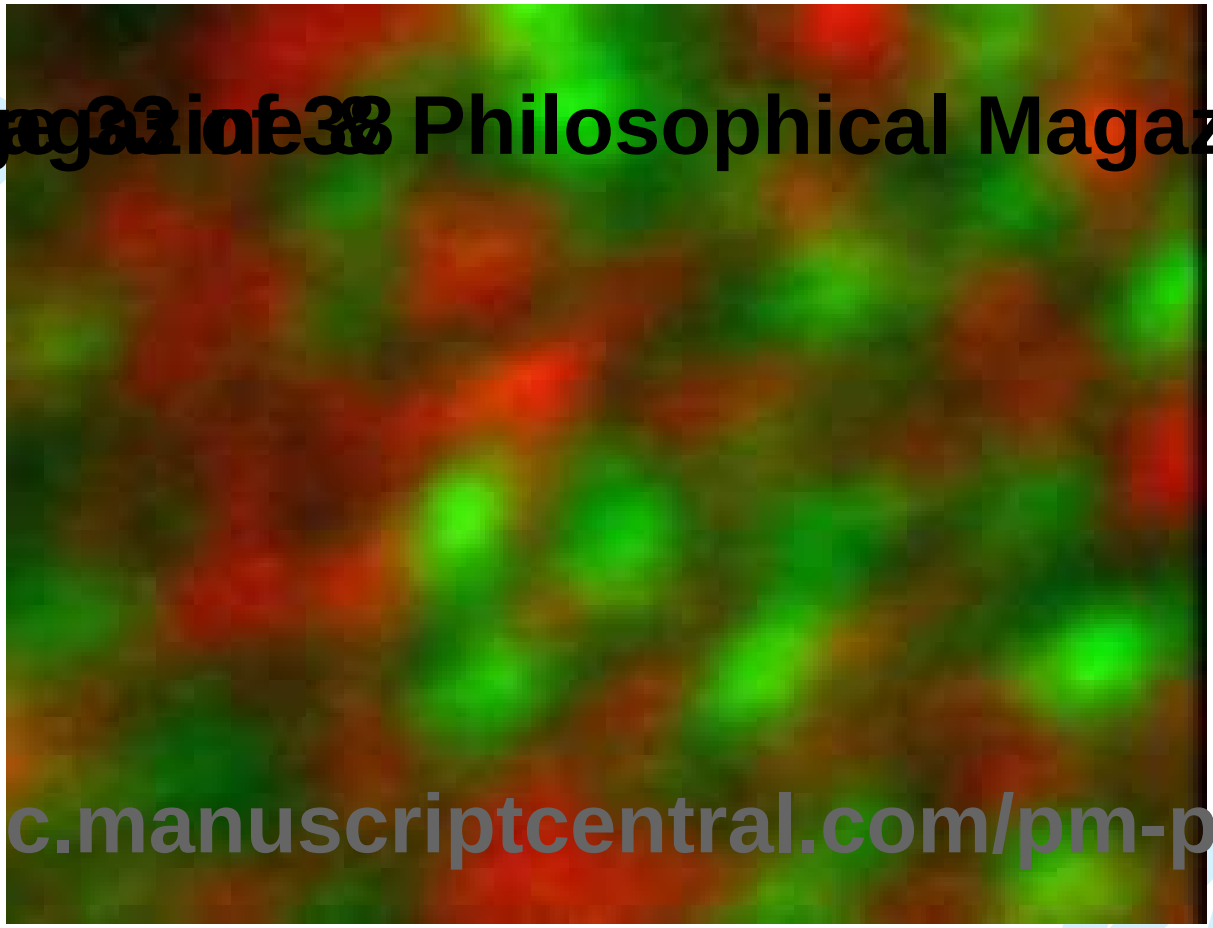

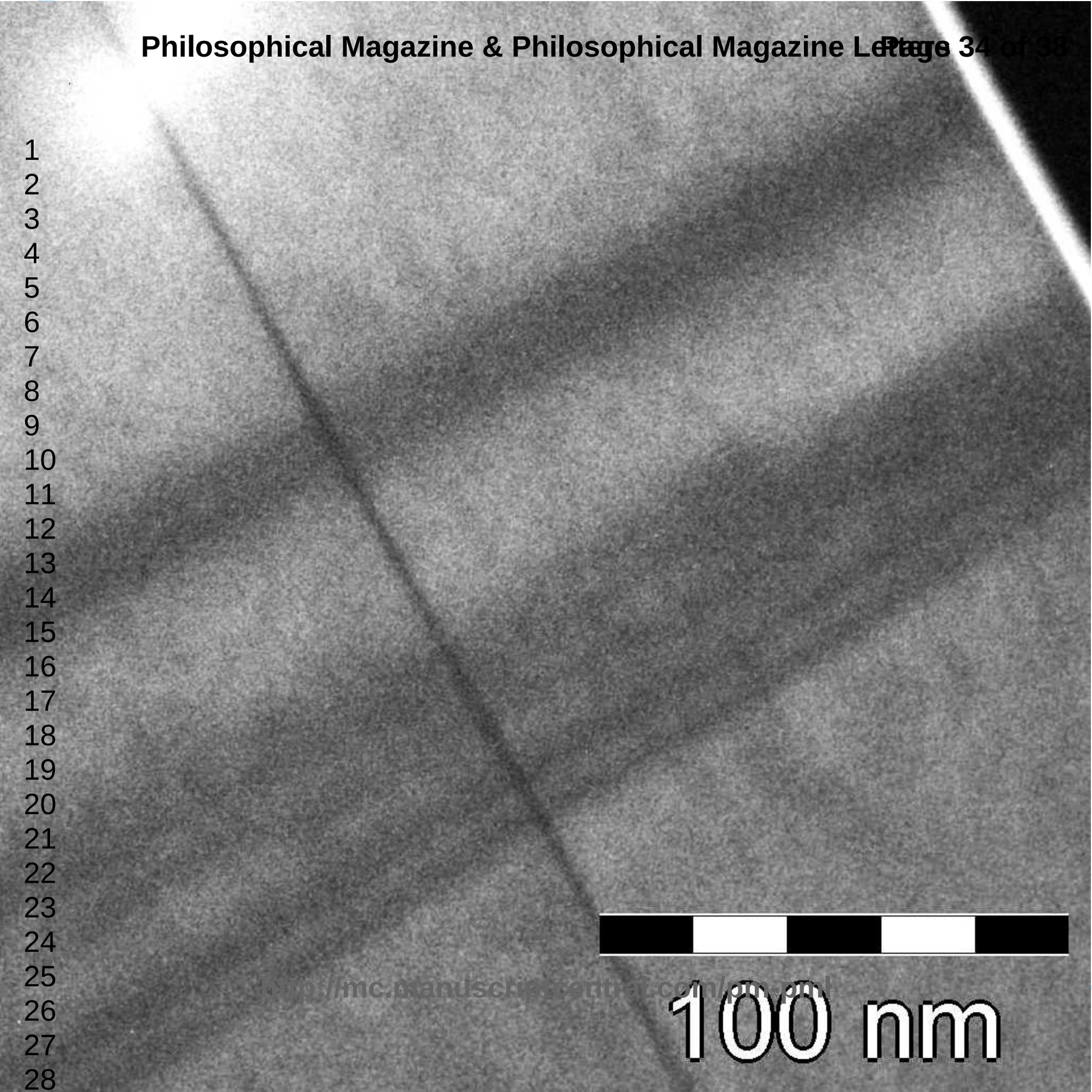

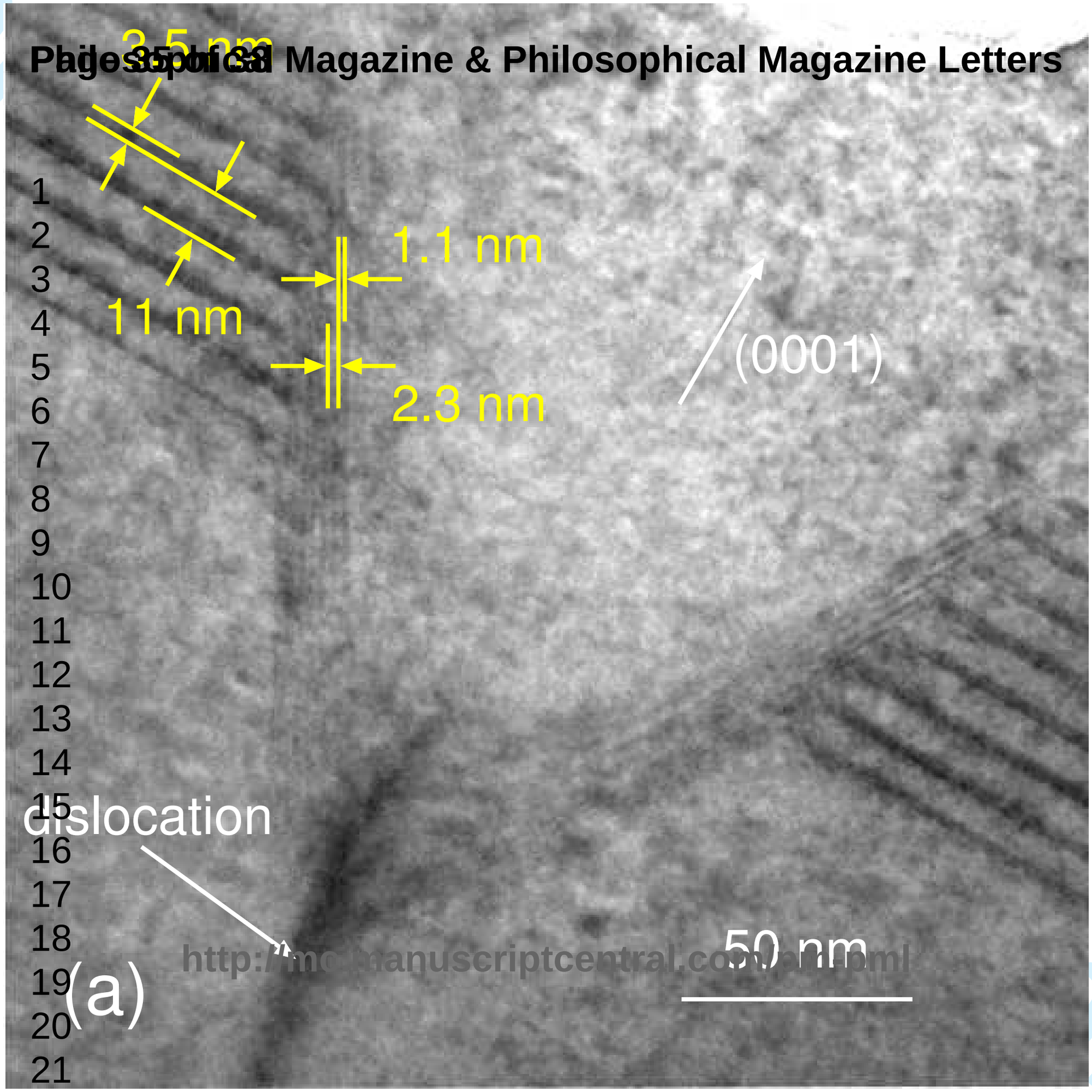

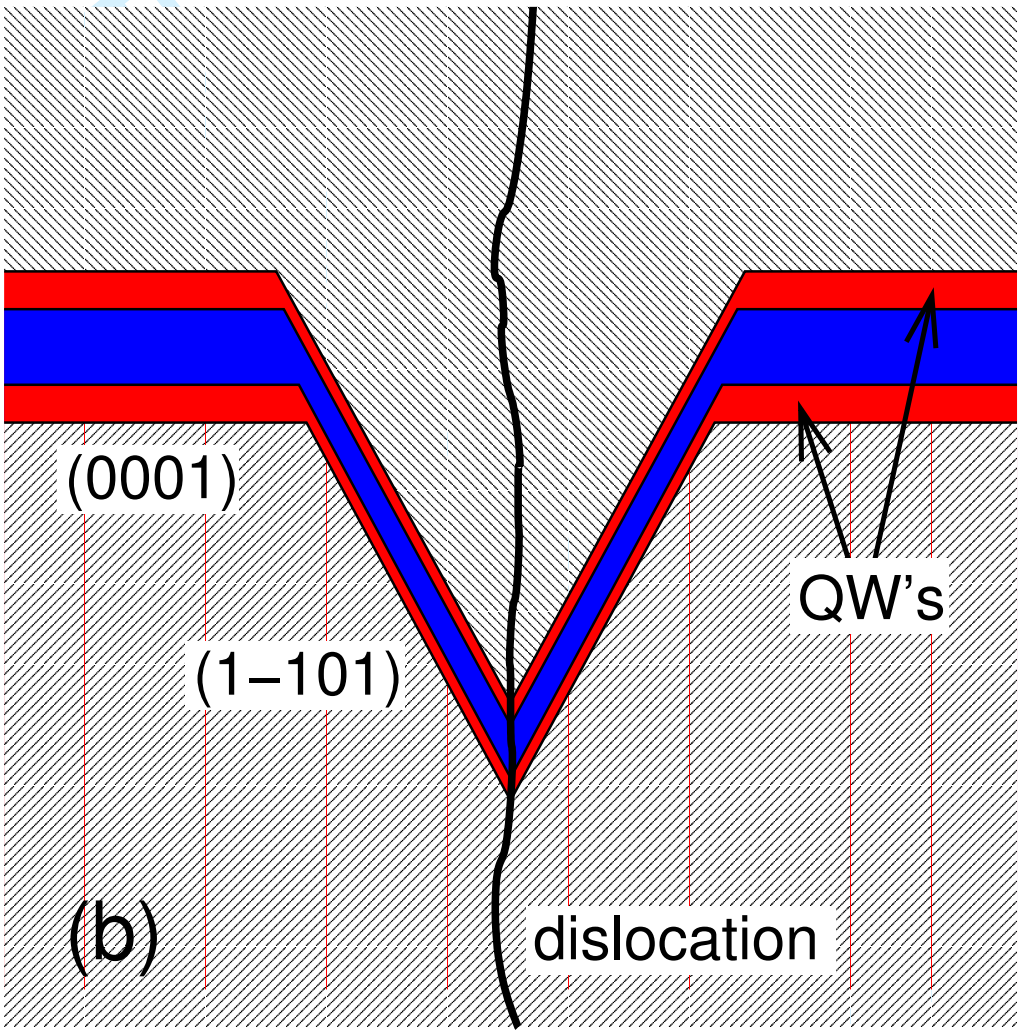
(0001)
(1–101)
QW's
(b)
dislocation

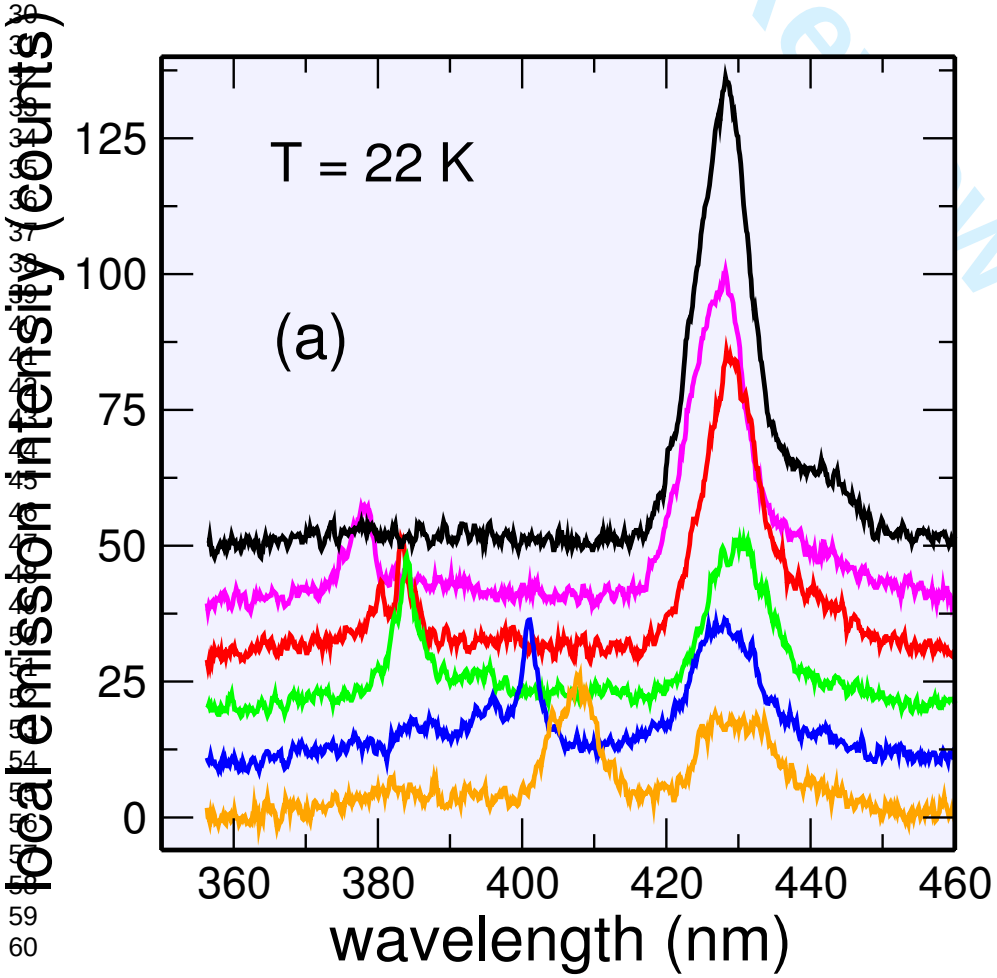

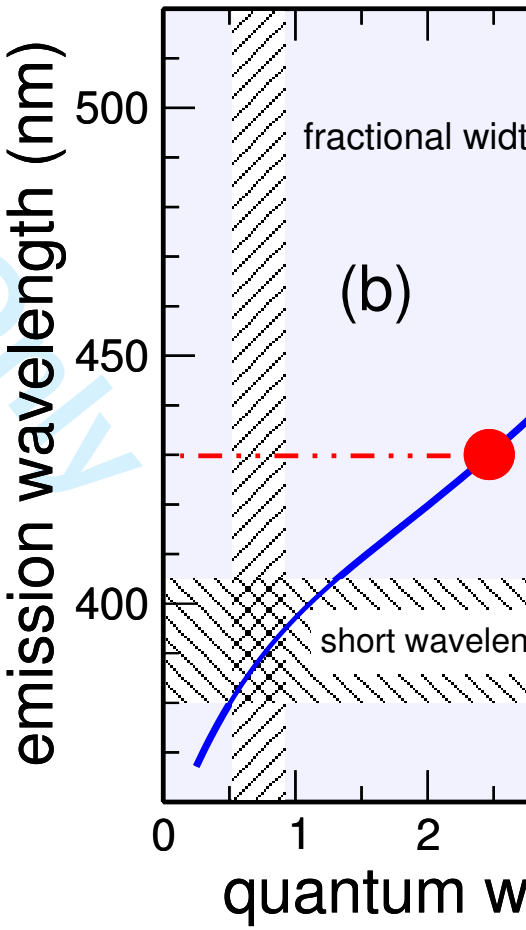

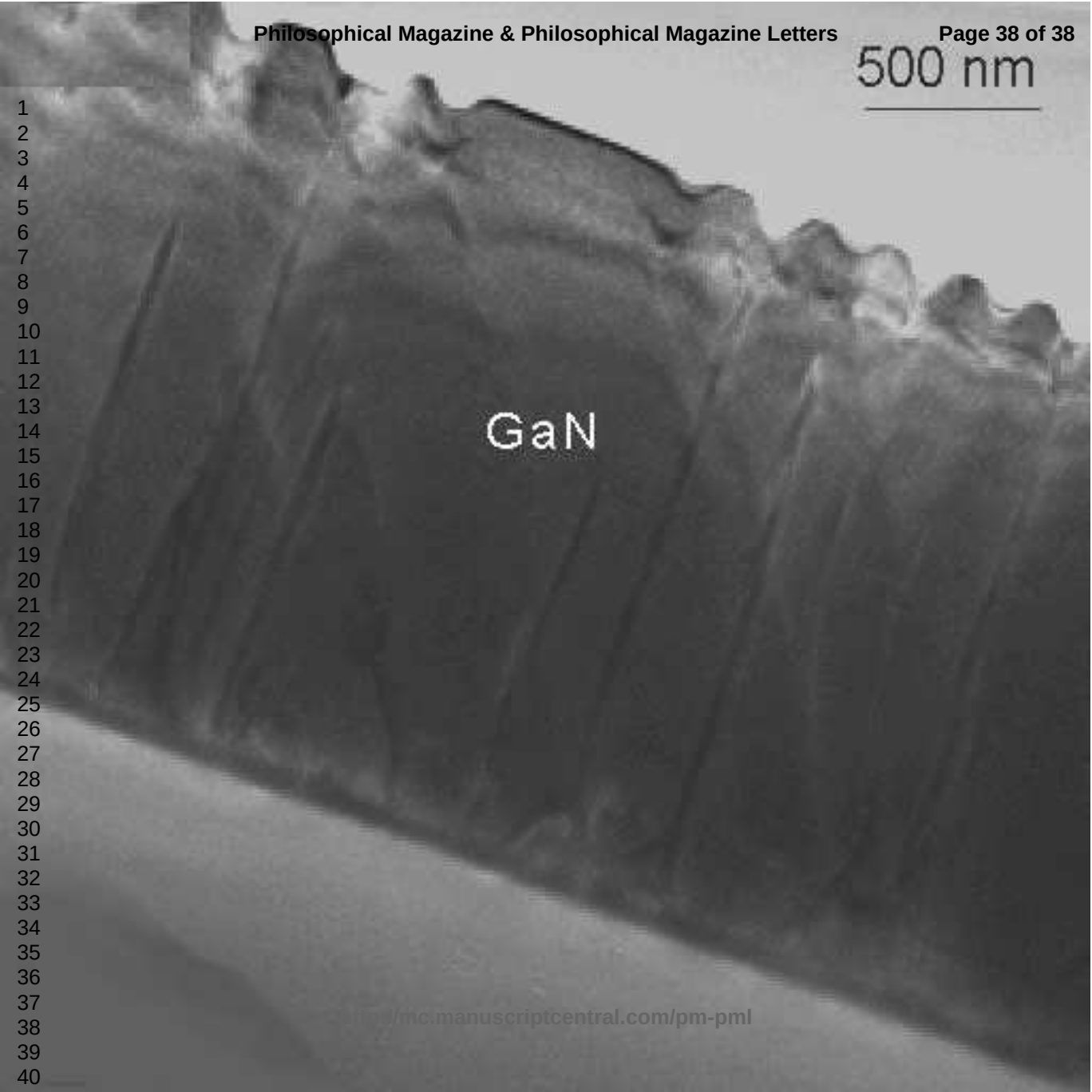

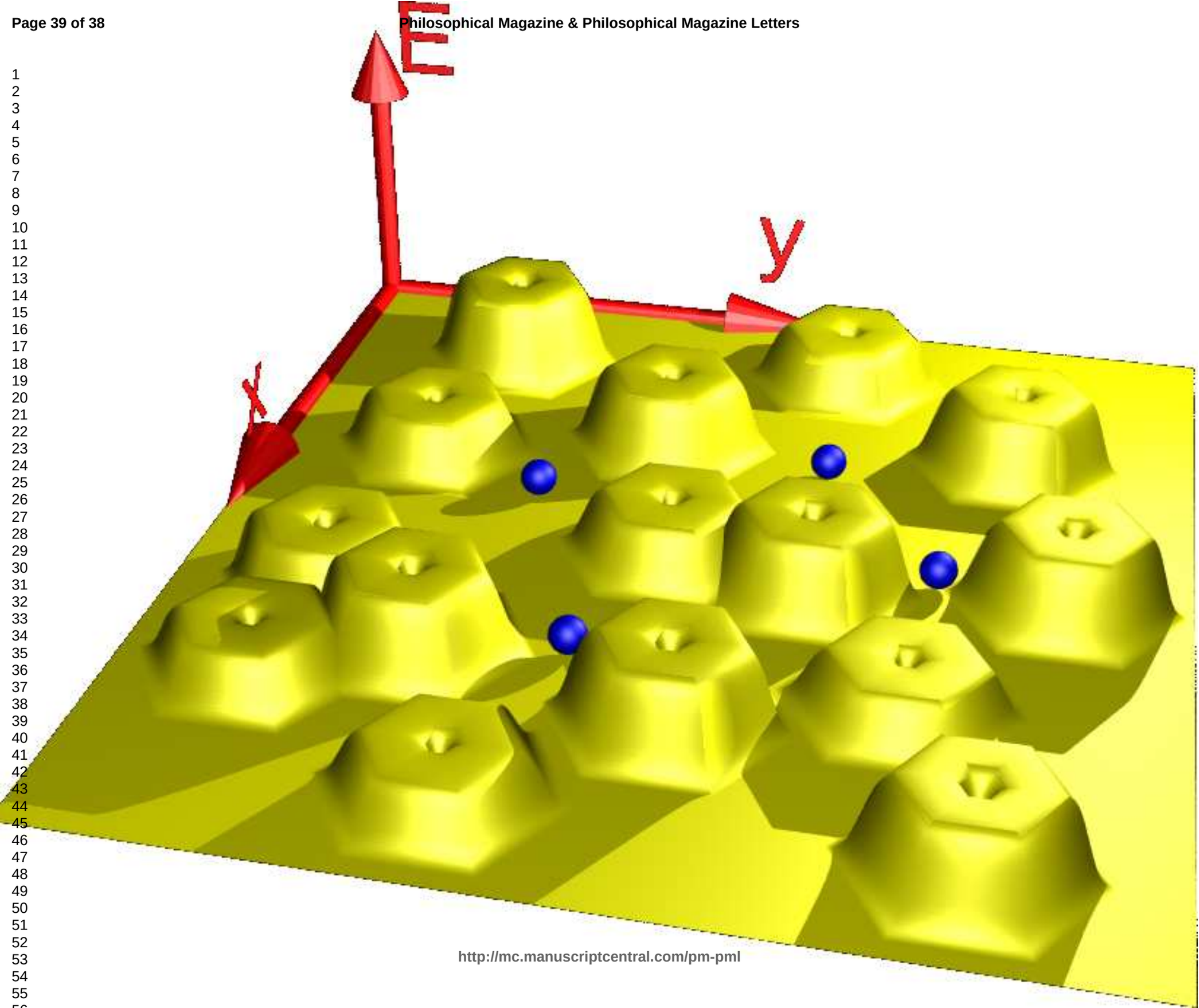
E
y
x